ANALYSIS OF CHANDRA DATA OF THE OLD CLASSICAL NOVA RR PIC (1925)

A THESIS SUBMITTED TO
THE GRADUATE SCHOOL OF NATURAL AND APPLIED SCIENCES
OF
THE MIDDLE EAST TECHNICAL UNIVERSITY

BY

YAKUP PEKÖN

IN PARTIAL FULFILLMENT OF THE REQUIREMENTS
FOR
THE DEGREE OF MASTER OF SCIENCE
IN
PHYSICS

SEPTEMBER 2007

Approval of the Thesis

"ANALYSIS OF CHANDRA DATA OF THE OLD CLASSICAL NOVA RR PIC (1925)"

Submitted by **YAKUP PEKÖN** in partial fulfillment of the requirements for the degree of **in Physics** by,

Dean, Graduate School of _____

Head of Department, **Physics** _____

Assoc. Prof. Dr. Şölen Balman
Supervisor, **Physics Dept.,METU** _____

Examining Committee Members:

Prof. Dr. Nilgün Kızıloğlu(*)
Physics Dept., METU _____

Assoc. Prof. Dr. Şölen Balman(**)
Physics Dept., METU _____

Prof. Dr. Halil Kırbıyık
Physics Dept., METU _____

Prof. Dr. Ümit Kızıloğlu
Physics Dept., METU _____

Assist. Prof. Dr. S. Çağdaş İnam
Electric and Electronical Engineering Dept., BAŞKENT U. _____

Date: _____

(*) Head of Examining Committee
(**) Supervisor

I hereby declare that all information in this document has been obtained and presented in accordance with academic rules and ethical conduct. I also declare that, as required by these rules and conduct, I have fully cited and referenced all material and results that are not original to this work.

Name, Last Name : YAKUP PEKÖN

Signature :

ABSTRACT

ANALYSIS OF CHANDRA DATA OF THE OLD CLASSICAL NOVA RR PIC (1925)

PEKÖN, YAKUP

M.S., Department of Physics

Supervisor: Assoc. Prof. Dr. Şölen Balman

September 2007, 58 pages

In this work, the *CHANDRA* ACIS-S3 data of the old classical nova RR Pic (1925) is presented. The source is detected with a count rate of 0.067±0.002 c/s in the 0.3-5.0 keV energy range. The orbital period of the binary system in X-ray wavelengths is detected. X-ray spectrum of RR Pic can be represented by a composite model of bremsstrahlung with a photoelectric absorption, two absorption lines centered around 1.1-1.4 keV and 5 Gaussian emission lines centered at around 0.3-1.1 keV . The best fit bremsstrahlung temperature derived from the model ranges from 0.99 to 1.60 keV and the unabsorbed X-ray flux is found to be $2.51^{+0.39}_{-1.21}$ erg cm^{-2} s^{-1} in the 0.3-5.0 keV range.The absorption lines correspond to several transitions of Fe, Ne and Na. The emission lines correspond to various transitions of S, N, O, C, Ne and Fe ; and observations with better spectral resolution are needed to determine the exact transitions. The source spectrum is better explained with photoionized plasma model rather than the cooling flow model. It has also been found that the neutral Hydrogen column density differs for orbital minimum and orbital maximum spectra with

values $0.25^{+0.23}_{-0.18}\times10^{22}$ atoms/cm^2 and $0.64^{+0.13}_{-0.14}\times10^{22}$ atoms/cm^2 respectively at 3σ confidence level. The difference of neutral Hydrogen column density between the maximum and minimum phase spectra indicates existence of a warm absorbing region on the disc at the location of the impact zone.

Keywords: Cataclysmic Variables, Novae, X-rays, Spectral Analysis, RR Pic

ÖZ

ESKİ KLASİK NOVA RR PIC'İN (1925) CHANDRA VERİLERİNİN ANALİZİ

PEKÖN, YAKUP

Yüksek Lisans, Fizik Bölümü

Tez Yöneticisi: Doç. Dr. Şölen Balman

Eylül 2007, 58 sayfa

Bu çalışmada eski bir klasik nova olan RR Pic'in (1925) CHANDRA ACIS-S3 verilerinin analizi sunulmaktadır. Kaynak 0.3-0.5 keV enerji aralığında 0.067 ± 0.002 c/s sayma oranıyla gözlenmiştir. Çift yıldız sisteminin yörünge periyodu X-ışını dalgaboylarında bulunmuştur. RR Pic'in X-ışını tayfı bremsstrahlung, fotoelektrik soğurma, 1.1-1.4 keV aralığında iki soğurma çizgisi ve 0.3-1.1 keV aralığında 5 Gaussian salma çizgisi ile ifade edilebilmektedir. Modele en uygun bremsstrahlung sıcaklığı 0.99-1.60 keV aralığında olup, kaynağın soğurulmamış akısı 0.3-0.5 keV enerji aralığında $2.51^{+0.39}_{-1.21}$ erg cm^{-2} s^{-1} olarak bulunmuştur. Soğurma çizgileri Fe, Ne ve Na elementlerinin çeşitli geçişlerine tekabül etmektedir. Salma çizgileri ise S, N, O, C, Ne ve Fe elementlerinin çeşitli geçişlerine tekabül etmektedir. Kesin geçişleri belirlemek için daha iyi tayf çözünürlüklü gözlemlere ihtiyaç vardır. Kaynak tayfı soğuyan akış modelinden ziyade fotoiyonize plazma modeli ile daha iyi açıklanabilmektedir. Nötr hidrojen kolon yoğunluğu faz çözünürlüklü tayf çalışmasında, minimum ve maksimum akıya denk gelen tayflar için 3σ güvenilirlik aralığında sırasıyla $0.25^{+0.23}_{-0.18} \times 10^{22}$

atom/cm^2 and $0.64^{+0.13}_{-0.14}\times10^{22}$ atom/cm^2 olarak değişim göstermektedir. Nötr hidrojen kolon yoğunluğunda görülen bu fark diskin üzerinde kesişme bölgesinde sıcak bir soğurma bölgesinin bulunduğuna işaret etmektedir.

Anahtar Kelimeler: Kataklismik Değişkenler, Novalar, X-Işınları, Tayf Analizi, RR Pic

ACKNOWLEDGMENTS

I would like to express my deep and sincere gratitude to my supervisor Assoc. Prof. Dr. Şölen Balman for her guidance, encouragement and understanding throughout this research.

I thank my colleagues and friends in METU Astrophysics Group for their support and friendship.

I especially thank Tuğba Adalı for her love and understanding all these years.

I acknowledge support from TÜBİTAK, The Scientific and Technological Research Council of Turkey, through project 106T040.

TABLE OF CONTENTS

ABSTRACT iv
ÖZ vi
ACKNOWLEDGMENTS viii
TABLE OF CONTENTS ix
LIST OF TABLES xi
LIST OF FIGURES xii
CHAPTER

1 INTRODUCTION 1
1.1 Definition and Classification 1
1.2 Orbital Periods and Mass Accretion 3
1.2.1 Accretion in non-magnetic systems 6
1.2.2 Accretion in magnetic systems 9
1.3 Eruptive Behavior 11
1.3.1 Classical Nova Outbursts 11
1.3.2 Dwarf Nova Outbursts 12
1.3.3 Superoutbursts 13
1.4 X-rays From Cataclysmic Variables 14
1.4.1 Non magnetic Systems 17
1.4.2 Polars 21
1.4.3 Intermediate Polars 25

2 OBSERVATION AND DATA 29
2.1 The Source 29
2.2 Observation and Data Preparation 30
3 RESULTS 32
3.1 The CHANDRA Spectrum of the Point Source 32
3.2 Temporal Analysis of the Point Source 41
4 DISCUSSION 49
5 CONCLUSIONS 52
REFERENCES 53

LIST OF TABLES

TABLES

Table 3.1 Spectral parameters of the entire spectrum of the RR Pic in the energy range 0.3-5 keV. 33

Table 3.2 Spectral parameters of maximum and minimum spectra in the 0.3-5 keV region. 42

LIST OF FIGURES

FIGURES

Figure 1.1 The Roche equipotentials and Lagrange points 5
Figure 1.2 Formation of the Accretion Disc 7
Figure 1.3 Geometry of a non-magnetic CV 8
Figure 1.4 Geometry of an Intermediate Polar with an accretion disc 10
Figure 1.5 Geometry of a Polar 11
Figure 1.6 Graphic representation of the boundary layer in non-magnetic CVs 15
Figure 1.7 Graphic representation of the accretion column in magnetic CVs 16
Figure 1.8 ROSAT X-ray Light Curve of the Polar HU Aqr 24

Figure 3.1 The Spectrum Fitted with Simple Bremsstrahlung 35
Figure 3.2 The Spectrum Fitted with Bremsstrahlung and two Absorption Lines (GABS) 36
Figure 3.3 The Spectrum Fitted Bremsstrahlung with two Absorption Lines (GABS) and five Emission Lines (GAUSS) . . 37
Figure 3.4 The Spectrum Fitted with a (Bremsstrahlung + Blackbody) Model 38
Figure 3.5 The Spectrum Fitted with a (CEVMKL + Blackbody) Model 39
Figure 3.6 The Spectrum Fitted with VMCFLOW 40

Figure 3.7 The X-ray Light Curve of RR Pic 43
Figure 3.8 The Folded Light Curve of RR Pic 44
Figure 3.9 The Folded Light Curve of RR Pic 45
Figure 3.10 Simple Sine Function Fitted To the Folded Light Curve . 46
Figure 3.11 The Spectrum of the Maximum Phase 47
Figure 3.12 The Spectrum of the Minimum Phase 48

CHAPTER 1

INTRODUCTION

RR Pic is a binary system classified as a Cataclysmic Variable (CV). This chapter will provide a background information such as classification, physical properties, accretion process and outburst mechanisms on CVs in general. X-rays in CVs are particularly important, providing information about the accretion process.

1.1 Definition and Classification

CVs are compact binary systems consisting of a degenerate white dwarf and a low mass main sequence star. The white dwarf, which is the primary, accretes material from the main sequence star which is the donor or secondary (Warner, 1995).

The classification of CVs are based on their eruptive behavior and the strength of magnetic fields. Thus there is an orthogonal classification of CVs, dividing them into subgroups as Classical Novae, Dwarf Novae, Recurrent Novae and Nova-like Variables depending on their eruptive behavior which are *Non-Magnetic CVs*. *Magnetic CVs* are also divided into *Polars* and *Intermediate Polars* based on the magnetic field strength of the white dwarf. There is also overlap between subclasses such as some classical novae are also intermediate polars.

Classical Novae (CN), are CVs which show only one observed outburst.

During the outburst they can brighten up to 20 magnitudes. The amplitude of the outbursts are inversely correlated to the rate of fading after the outburst. The cause of these outbursts is the thermonuclear runaway of the hydrogen-rich material accreted by the white dwarf.

Dwarf Novae (DN) show outburst of 2-5 magnitude. These outbursts repeat themselves in a range of 10 days to tens of years. The outbursts are caused by the release of gravitational energy due to large rate of mass transfer increase on the disc. DN have three distinct subtypes based on the outburst structures:

Z Cam stars show prolonging standstills below the maximum brightness during which the outbursts cease in about 10 days to tens of years

Su UMa stars show additional superoutbursts and stays in outburst longer than normal outburst.

U Gem stars include all DN falling under neither of the above classes

Recurrent Novae (RN) are like CN but show multiple outbursts.

Nova-like Variables (NL) are the CVs that have no outbursts. Since this is a contradicting definition, it is believed that NL consist of pro-novae, post-novae or possible Z Cam stars in standstill in which it may not be possible to observe the cataclysms due to our observational baseline which is about 100 years. (Warner 1995)

Non-Magnetic CVs include all the CVs in which the magnetic field of the white dwarf B$\leq 10^4$ Gauss. The mass transfer to the white dwarf is achieved through an accretion stream and accretion disc.

Polars (AM Her stars) have white dwarfs with magnetic field strength B$>10^7$ Gauss. Because of the extremely strong magnetic field, accretion disc can not form in these systems. The accreted matter rather travels through an accretion stream and following the magnetic field lines, falls on the magnetic poles of the white dwarf.

Intermediate Polars (DQ Her stars) have magnetic fields in the 10^6-10^7 Gauss range. The accretion discs may form and they are disrupted by the presence of the magnetic field as the accreted material channel onto the field

lines of the white dwarf (Hellier, 2001).

CVs play important part in astrophysics for understanding the accretion process. Unlike other X-ray binaries, the discs of CVs are too cool to emit radiation in the X-ray range because of the relative shallowness of the potential well of the white dwarf. X-rays rather generate from the region where accretion takes place on the white dwarf. The X-rays do not affect the appearance of the accretion discs or the secular evolution of the systems. Therefore, accretion disc and accretion process can be independently studied in different wavelengths. Moreover, the high number of CVs in our galaxy and their closeness to earth provides observational advantages hence making the detailed studies in a wide wavelength range possible (Mukai, 2003).

1.2 Orbital Periods and Mass Accretion

Orbital period, P_{orb}, is the most and usually the only precisely known property of a CV. P_{orb} can provide information about the scale of the binary, allows categorizations between CV types and give an estimate about the evolution of the donor star.

Since CVs consist of two bodies bound by gravity orbiting roughly in a circular orbit around each other, they obey the Kepler's law. Hence, given their orbital separation a, mass of the primary M_1, and mass of the secondary M_2, orbital period of the system P_{orb} can be found with the following relation.

$$P_{orb}^2 = \frac{4\pi^2 a^3}{G(M_1 + M_2)} \tag{1.1}$$

Rearranging the terms in Equation 1.1 one can get the orbital separation as

$$a = 3.53 \times 10^{10} P_{orb}^{2/3} M^{1/3} (1+q)^{1/3} \ \text{cm} \tag{1.2}$$

where q is the mass ratio M_2/M_1 , M is $M_1/\mathrm{M}_\odot$ and P_{orb} is given in hours. Taking values $\mathrm{M}_1=\mathrm{M}_2=\mathrm{M}_\odot$ and P_{orb}=1-10, we get binary separations around 0.5-3 $\mathrm{R}_\odot$ which implies CVs are close binaries.

Majority of the CVs have orbital periods P_{orb} between 75 min and 8 hours. These systems consist of Roche Lobe-filling main sequence stars and a white dwarf. However the number is scarce in the 2-3 region which is called the *period gap*. The period gap is associated with switching from magnetic breaking to gravitational radiation as the system evolves to lower P_{orb}. There are systems with P_{orb} in the 8h-3d range with evolved subgiants as donors. Some CVs have P_{orb} 200d which require their donors to be giants. There exist systems with P_{orb} beyond 200 d, called symbiotic binaries, but these generally do not have Roche Lobe-filling secondaries, rather consist of a white dwarf orbiting in the wind of a supergiant. In the region below 75 min there exist a class called AM CVn stars with Helium rich degenerate donors (Hellier 2001, Kuulkers et al. 2006, Nelemans 2005).

Since CVs are close binaries, their interaction is more complex than that of two point masses. Tidal interactions combining with gravitational and centrifugal effects take place, distorting the secondary star and causing it to rotate synchronously with the orbital motion. Tidal effects enable us to simplify the systems to have circular orbits and apply the Kepler's law (Equation 1.1).

During the evolutionary sequence, the secondary star expands until material can no longer be bounded by the secondary and at some point accretes to the white dwarf. The process is called Roche lobe overflow. For a free particle moving in a rotating reference system, it is the analysis of a restricted three body problem. The Roche lobe potential,

$$\Phi(\vec{R}) = -\frac{GM_1}{\left|\vec{R}-\vec{R}_1\right|} - \frac{GM_2}{\left|\vec{R}-\vec{R}_2\right|} - \frac{1}{2}(\vec{\Omega}\times\vec{R})^2 \tag{1.3}$$

where Ω is the angular frequency of the orbit, signifies the gravitational effect of the two stars on a third object. Using Roche potentials one can plot the equilibrium surfaces and equilibrium points (Lagrange points) in the system as in Figure 1.

The innermost teardrop shape surface is the Roche Lobe and the point adjoining the two Roche lobes of the stars is called the *inner lagrangian point*

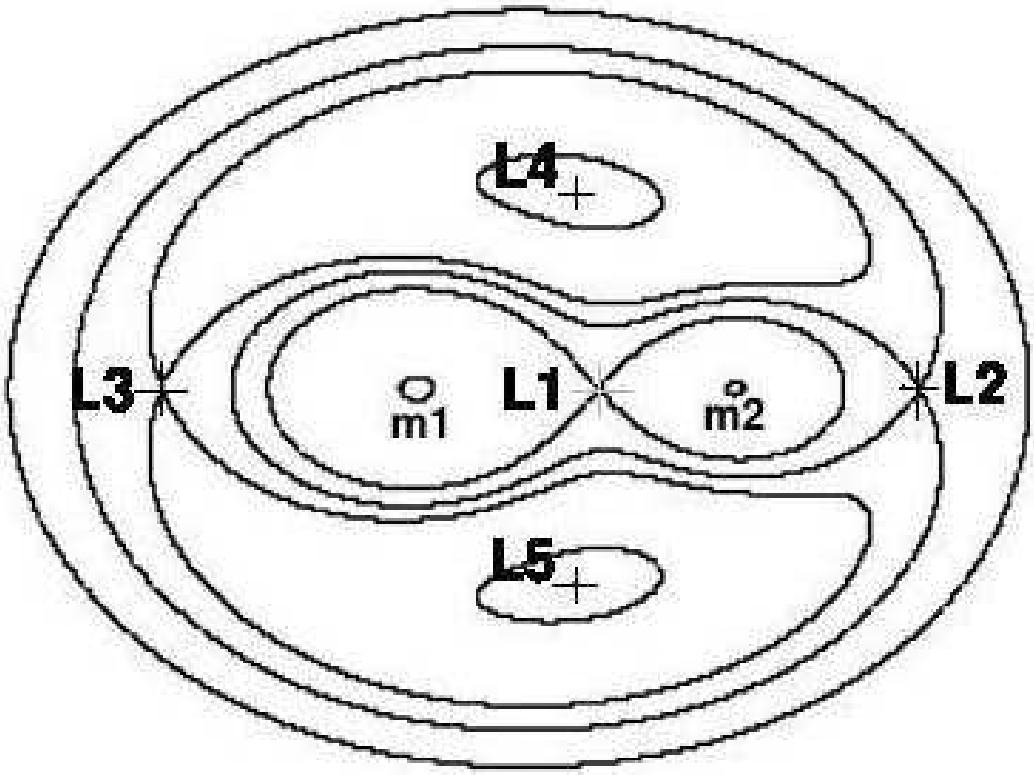

Figure 1.1: The Roche equipotentials and Lagrange points

(The lines represent the equipotentials, points L1 to L5 are the equilibrium points (Lagrangian points), m1 and m2 are the white dwarf and the secondary respectively. Adapted from Hellier (2001))

or L_1. When the secondary star expands, it fills its Roche lobe and cannot expand any longer. The material flows out of L_1 into the Roche lobe of the white dwarf. Since the white dwarf has not filled its Roche lobe the material will flow inwards and accrete on the white dwarf.

For steady mass accretion, the binary system loses its angular momentum reducing the size of the Roche lobe so that the secondary does not have to expand to a greater extent. There are two mechanisms to allow the loss of angular momentum: gravitational radiation and magnetic braking. *Gravitational radiation* occurs in close orbiting CVs releasing the gravitational energy and reducing the orbit size. *Magnetic braking* occurs when stellar wind (ionized

particles) from the secondary rotates and accelerates along with its magnetic field lines and ejects out of the system carrying the angular momentum out. The loss of angular momentum brakes the rotation of the secondary. However tidal forces ensure the secondary to corotate with the orbital motion and hence the angular momentum loss is supplied by the system by shrinking the orbit.

The accretion process and geometry of CVs are determined by the magnetic field strength of the white dwarf. So we examine the accretion as *accretion in non-magnetic systems* and *accretion in magnetic systems*.

1.2.1 Accretion in non-magnetic systems

The accreted material shoots out of L_1 at supersonic speeds more than 100 km/s. Because of the rotation of the Roche lobe, the velocity has a lateral component, therefore does not directly fall on to the white dwarf. The stream of material moves in a path close to white dwarf and whirls around and settles into a circular orbit (on *circulisation radius*) with the same angular momentum it has on L_1 forming a ring. The inner parts of the ring move faster obeying the Kepler's law thus causing friction with the outer parts of the ring radiating the gravitational energy away. Having lost some energy, material in the inner part of the disc moves in smaller orbits, consecutively material in the outer ring rotates in a larger orbit to conserve the angular momentum, and thus the ring spreads out to become a thin disc which is called the *accretion disc* (See Figure 1.2) (Verbunt 1982, Hellier 2001). Standard accretion disc theory attributes the angular momentum transfer to the viscosity of the disc, such that disc is composed of annuli exchanging blobs of material due to viscosity. Viscosity, dominating the flow of material through the disc is parametrised by Shakura & Sunyaev (1973) as

$$\nu = \alpha c_s H \tag{1.4}$$

where ν is the viscosity, α is a constant less than 1, c_s is the speed of sound and H is the thickness of the disc.

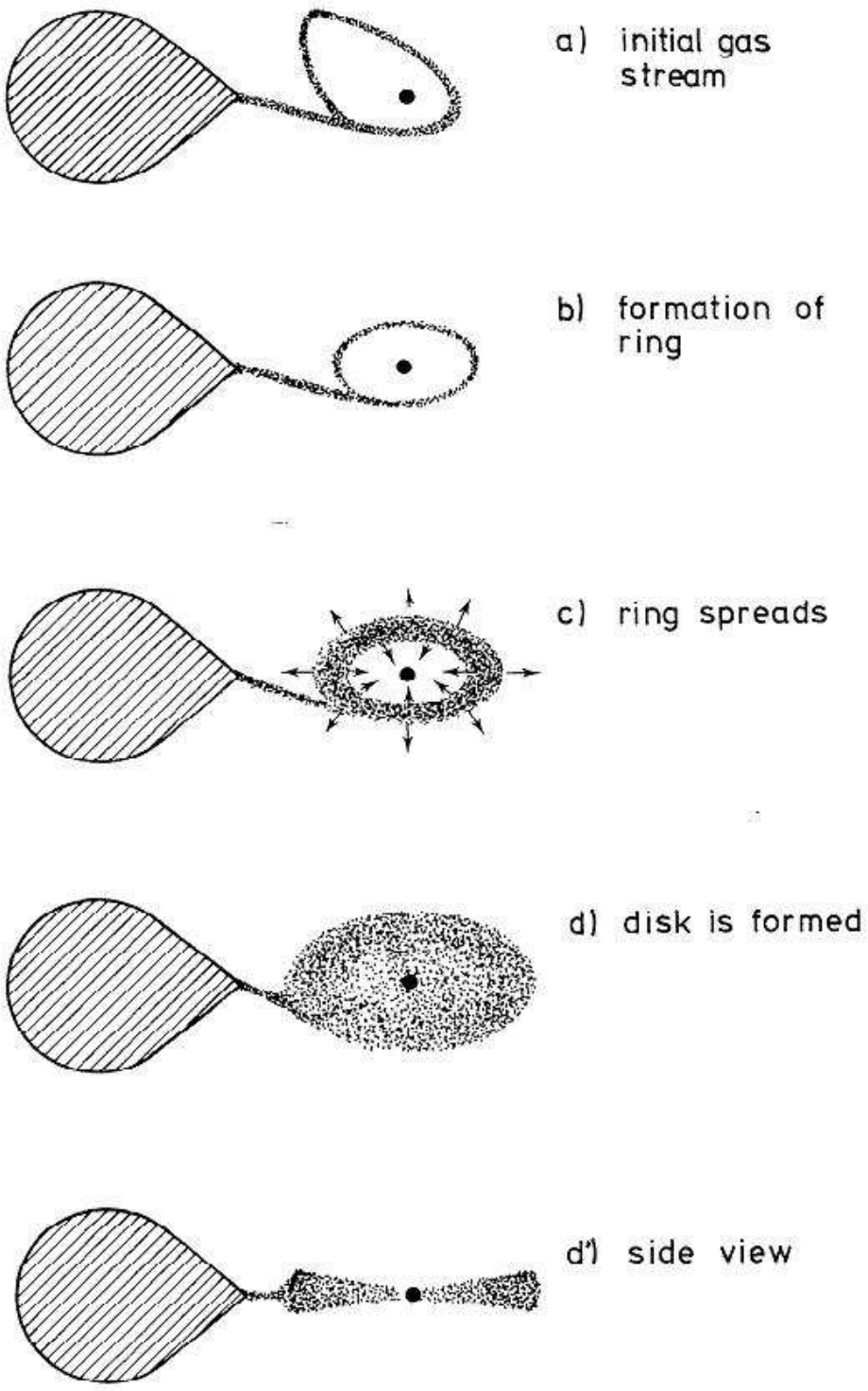

Figure 1.2: Formation of the Accretion Disc

(Figure taken from Warner (1995))

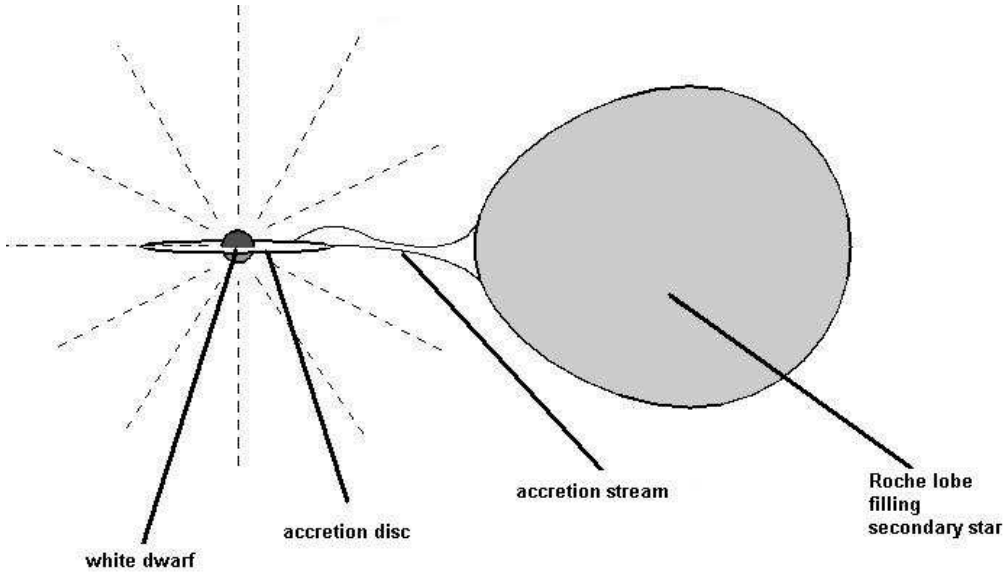

Figure 1.3: Geometry of a non-magnetic CV

(Figure taken from http://www.physics.usyd.edu.au/rcfta/anrep93/node22.html)

The rim of the disc is bound by the tidal interactions with the secondary. The location where the material stream from the secondary intersects the accretion disc is called the *bright spot*. Here the impact of particles at supersonic speeds on to the disc causes a shock-heated region which radiates brightly in the optical region. The inner part part of the disc extends until it comes to contact with the white dwarf. The material on this inner part accretes on to the white dwarf and the innermost region of the disc where the accretion takes place is called the *boundary layer*. The accretion disc lies on the orbital plane. Accretion discs have a temperature of about 5000 K on the rim and gets hotter toward the inner disc up to 100000 K. They emit radiation in a range of IR to X-rays due to loss of gravitational energy of the particles (Hellier 2001, Hamilton et al. 2007).

1.2.2 Accretion in magnetic systems

In the case of strong magnetic field of the white dwarf, the accretion process differs. The material moving out of the Roche lobe of the secondary follows a projectile motion as in non-magnetic case but this time magnetic field deters the motion. The effect of the magnetic field depends on the Alfvèn radius where the kinetic energy density of the material is roughly equal to the magnetic energy density and given as

$$R_A = 3.7 \times 10^9 \dot{M}_{17}^{-2/7} M_{\odot}^{-1/7} \mu_{32}^{4/7} \text{ cm} \tag{1.5}$$

where $\dot{M}_{17}$ is the accretion rate in units of 10^{17} g/s, $M_{\odot}$is the mass of the white dwarf in terms of solar mass and μ_{32} is magnetic moment of the white dwarf in 10^{32} G cm^3 (Patterson 1994). Accreted material lying within Alfvèn radius is affected by the magnetic fields more than ram pressure. Here, the particles follow the magnetic field lines and accrete on to the white dwarf.

If the magnetic field strength (B) is greater than about 10^7 G (as in polars) then Alfvèn radius extends outside the *circulisation radius* (in extremely strong magnetic fields, it may exceed up to L_1) and hence the accretion disc can not form. The transferred material locks to the field lines and co-rotate with the white dwarf and the white dwarfs spin period synchronizes with the orbital period. The material then falls on to one or two magnetic poles of the white dwarf. It forms *accretion columns* rather than the boundary layer. If the magnetic field B is in the range 10^6-10^7 G (as in intermediate polars) the accretion disc may form, inner parts of the disc is disrupted by the magnetic field and material accretes on to the magnetic poles as in the highly magnetic case. White dwarf synchronization does not occur due to weak magnetic field.

The magnetic axis do not align with the rotation axis in most cases. The system will act as an oblique rotator. The accretion column will encounter a stand off shock near the white dwarf surface and the shocked material will cool down as it reaches the white dwarf. Figure 1.3 and 1.4 show magnetic accretion with and without the accretion discs respectively.

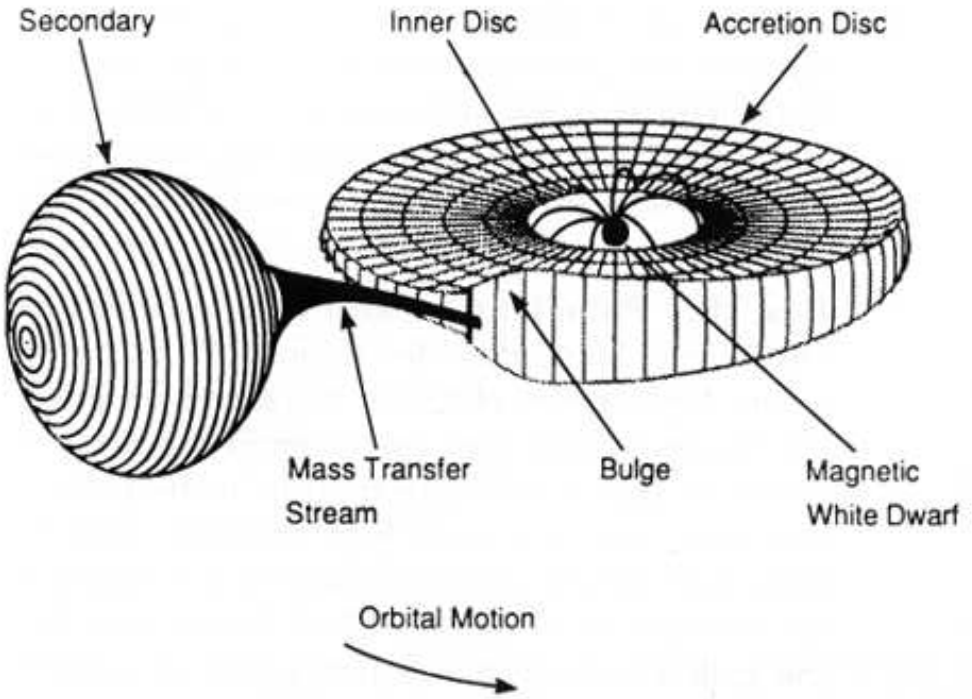

Figure 1.4: Geometry of an Intermediate Polar with an accretion disc

(Figure taken from
http://heasarc.gsfc.nasa.gov/docs/objects/cvs/cvstext.html#intermediate)

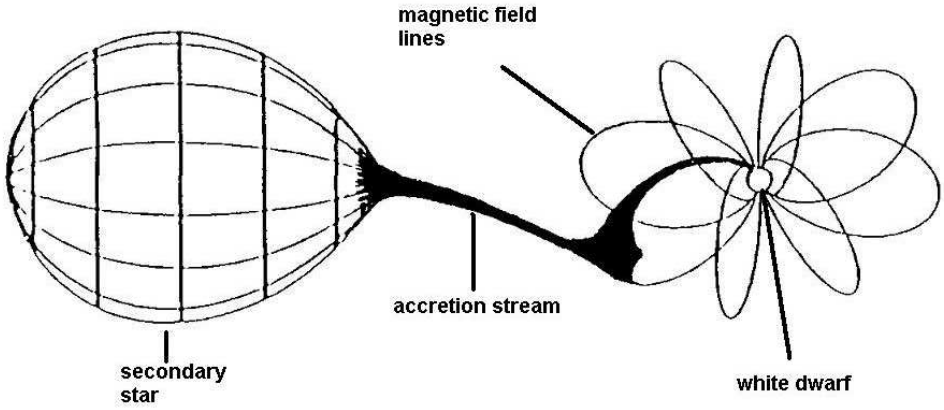

Figure 1.5: Geometry of a Polar

(Figure is taken from Cropper (1990))

1.3 Eruptive Behavior

The most distinctive and important phenomena displayed by cataclysmic variables are the outbursts. During the outburst, the brightness of the system increases dramatically and then decays. In this section, outbursts and the mechanisms responsible will be introduced.

1.3.1 Classical Nova Outbursts

Classical nova outbursts are explosions occurring on top of white dwarfs in cataclysmic variables due to a *thermonuclear runaway*.

White dwarfs are burnt out cores of stars that consumed most of its hydrogen into helium and other heavier elements. However, the accreted material from the secondary is mostly hydrogen and fresh hydrogen builds up on the surface as a layer. The density of the layer increases and the electrons become

degenerate and degeneracy pressure becomes dominant in the layer. As the layer thickens, temperature and density at the bottom of the layer increases sufficient enough for hydrogen fusion. As the hydrogen burns into helium the released energy does not cause thermal expansion. The dominant pressure is degeneracy pressure which is independent of temperature. The temperature and reaction rate increases reciprocally. As the temperature rises above 2x10^7 K, explosive hydrogen burning synthesizes unstable radioactive heavy elements which are convected to the surface. At some point the temperature is exceedingly high that the gas pressure overcomes the degeneracy pressure. Thus the material deposited at the outer shell expands out with speeds ~3000 km/s as the energy is released. (Hellier 2001)

The accretion rates should be low enough ($\dot{M} \sim 10^{-9}$-10^{-10} $M_\odot$ yr^{-1}) so that the degeneracy condition is supplied. After the outburst, the white dwarf will be hydrogen deficient again and the whole process will repeat itself with in 10^4 - 10^5 years. The outburst will result in an increase in the luminosity of the system which corresponds to a decrease of apparent visual magnitude of more than 9 magnitudes occurring in a few days, with a pre-maximum halt, 2 magnitudes before maximum, in some cases. Nova light curves are classified according to their speed class, defined from either t_2 or t_3, which is the time needed to decay by 2 or 3 visual magnitudes after maximum. The brightness and decay times are inversely related (Hernanz 2005).

1.3.2 Dwarf Nova Outbursts

Dwarf nova outbursts are different than the nova outbursts by mechanism and nature of the outbursts. The energy source is simply the gravitational field of the white dwarf unlike thermonuclear runaway on the surface of the white dwarf. Basically due to instabilities in the accretion disc, mass accumulates on the disc and when the critical density is reached, accumulated mass moves rapidly on to the white dwarf releasing significant amount of energy causing the outbursts.

Dwarf nova outbursts repeat themselves in an *outburst cycle*. As stated before viscosity ν governs the mass flow F_M through the disc. If $F_M > \dot{M}$ then then mass will accumulate on the disc, if $F_M < \dot{M}$ then the disc will be depleted. However, dependence of viscosity on density is different at different temperatures. At low temperatures, viscosity increases with increasing density and energy transfer is due to convection. At higher temperatures viscosity decreases with increasing density and energy transport is due to radiation. In the quiescence state, $\dot{M}$ is higher than F_M enough to accumulate matter in the disc, and density of the disc increases. At some point matter becomes thermally unstable boosting viscosity and the density dependence of viscosity reverses and F_M exceeds $\dot{M}$ hence spreads the excess material onto outer disc and towards the white dwarf causing outburst. The spreading of mass continues gradually after the outburst until quiescence state is reached and $F_M < \dot{M}$ and the cycle starts over.

The outbursts show much variety in shape, magnitude and duration even within the same source. The magnitude change is around 2-5 and recurrence times are in a wide range of a few days to tens of years. The outburst profile differ as well. The rise to maximum can be rapid or slow depending on the outburst happening from outside-in or inside-out. The peak can show a plateau-like structure when the entire disc is in outburst. The declines all show similar gradual decays. (Hellier 2001, Warner 1995, Smith 2007)

1.3.3 Superoutbursts

SU UMa stars show superoutbursts additional to outbursts other dwarf novae exhibit. The normal outburst mechanism is the same but in SU Uma stars the mass lost to white dwarf is much less causing the disc to grow in size in every outburst cycle. When the disc radius reaches the *resonant radius* where particles have orbital frequency $\Omega = 3\Omega_{orb}$, the tidal forces are dominant on the disc so that the disc precesses. The eccentric disc can then loose enough angular momentum through spreading out the excess mass and shrink back to

small symmetric disc. Thus the superoutbursts occur. The disc grows again due to normal outbursts and superoutbursts repeat themselves in a *supercycle*.

Superoutbursts occur less frequently than normal outbursts. The recurrence time varies from several hundred to several thousand days. The superoutburst last about two weeks where normal outburst last about a few days and also have higher amplitudes. During the superoutbursts, the orbital light curve shows *superhumps* ; periodic photometric light humps with amplitudes about 0.2-0.3 mag. The superhumps are seen due to the asymmetry of the disc. (Osaki 1996)

1.4 X-rays From Cataclysmic Variables

As stated previously, CVs emit X-rays due to accretion process, and studying X-ray properties helps us understand the accretion process and use the information in analogy with other accreting systems.

CVs emit radiation in a range of IR to X-rays and the accretion powered total luminosity is given by

$$L = \frac{G\dot{M}M}{R} \approx 2.2 \frac{\dot{M}}{10^{-9} M_{\odot} \mathrm{yr}^{-1}} \frac{M}{M_{\odot}} \frac{10^{4} \mathrm{km}}{R_{\odot}} L_{\odot} \tag{1.6}$$

where M and R are mass and radius of the white dwarf respectively. For CVs the total luminosity is about 10^{31} - 10^{34} erg s^{-1} with typical values given for accretion rate, mass and radius of the white dwarf.

X-rays originate mainly in the region where the accreted material settles on the surface of the white dwarf for non-magnetic systems, the boundary layer, for magnetic systems the accretion column; hence accretion geometry affects the origin and properties of emitted X-rays.

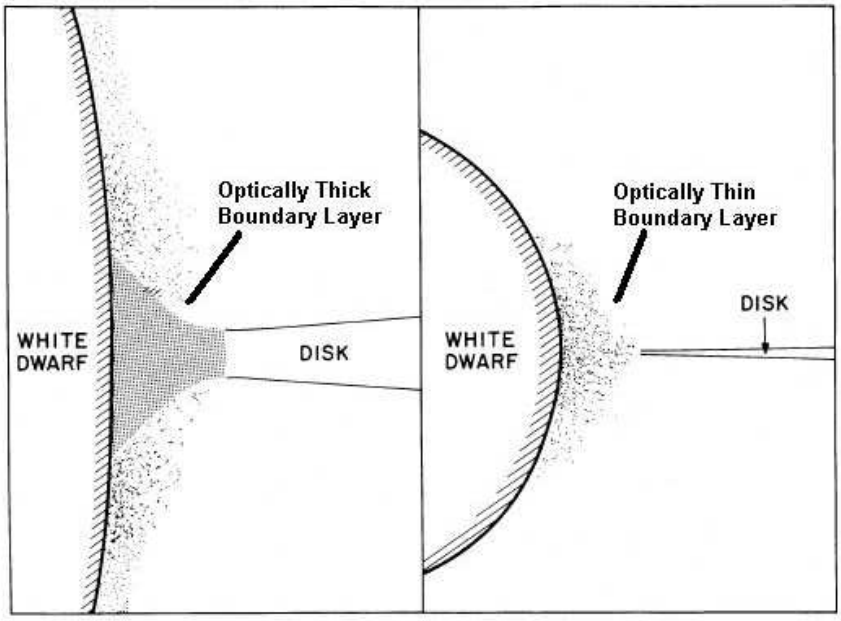

Figure 1.6: Graphic representation of the boundary layer in non-magnetic CVs

(The box on the left shows the optically thick boundary layer when the system's $\dot{M}$ is high ($>10^{16}$ gr/s) and on the box on the right shows the optically thin boundary layer where $\dot{M}$ is low ($<10^{16}$ gr/s. Adapted from Patterson & Raymond (1985).)

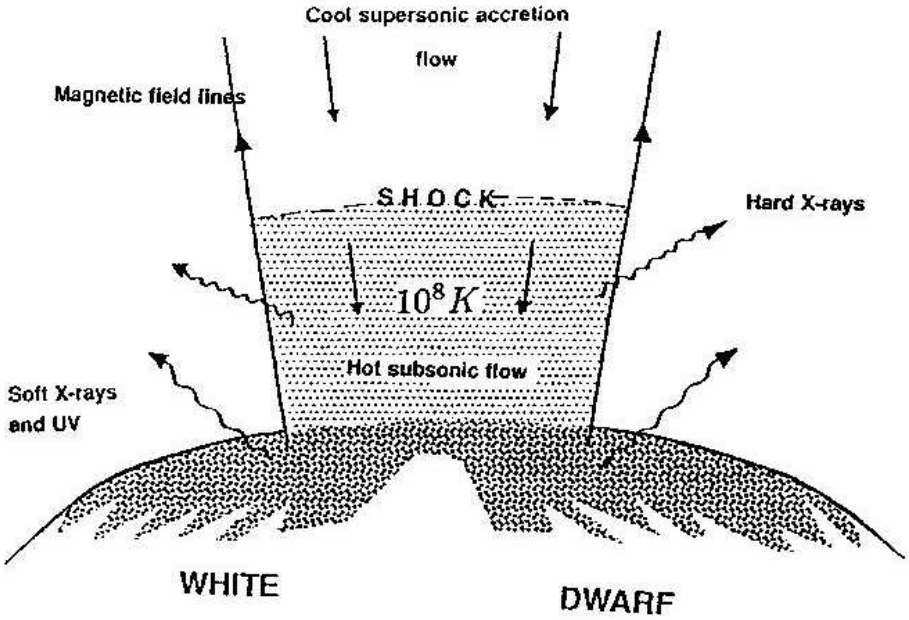

Figure 1.7: Graphic representation of the accretion column in magnetic CVs

(The figure also shows how soft and hard X-rays emerge from the accretion column. Adapted from Patterson (1994).)

1.4.1 Non magnetic Systems

Origin of X-rays

In Non-magnetic CVs, where B is less than about 10^4 Gauss, the accreted material from the donor forms an accretion disc. The material on the disc then falls on to the white dwarf via the boundary layer. Generally, half of the total luminosity is due to loss of gravitational energy on the disc while the other half is due to the loss in the boundary layer (Pringle 1981). The particles on the boundary layer moves with Keplerian velocities which is much higher than the rotation velocity of the white dwarf. The material in the disc is slowed down in order to accrete on to the white dwarf in a shock that produces X-rays in the post-shock regions. The X-ray luminosities are usually 10^{30} - 10^{32} erg/s (Baskill et al. 2005). These luminosities are small enough not to disturb the appearance of the disc. Since the disc has kT<1 eV it does not emit X-rays. It mainly radiates in optical and UV range. The boundary layer emits mostly in extreme UV and X-rays, so the main X-ray source of the CVs are the boundary layers (Kuulkers et al. 2006).

There may be other approaches to the X-ray emission such that the coronal X-ray emission from the donor or the hot spot powers the X-ray radiation. However, these ideas are not favorable due to some facts. First, the luminosities observed for the coronal X-rays are smaller than the most X-ray luminosity from the CVs. The bremsstrahlung temperatures observed for the coronal source spectra are also much smaller than the ones determined from CV spectra. The time scale for the coronal systems to vary is exceptionally larger than the CV data. As for the hot spot, the maximum temperature attainable is much smaller than the temperatures observed X-ray sources. Therefore the boundary layer approach explains the X-ray emissions best (Patterson & Raymond, 1985). However, there is a so called "missing boundary layer problem", the observed X-ray fluxes in most systems are quite lower than the expected. Several explanations for the lack of X-rays have developed such as reflection affects and

cooling flows or disruptions of the inner disk area by fast rotation of the WD, winds, coronal siphon flows, or magnetic fields (Ferland et al. 1982, Done & Osborne 1997, Warner et al. 1996, Meyer & Meyer-Hofmeister 1994)

The nature of the X-rays from the boundary layer depends on the accretion rate ($\dot{M}$) of the system. If $\dot{M}$ is smaller than the critical accretion rate, $\dot{M}_{critical}$ (10^{16} gr/s), then the accretion rate is low and the boundary layer will be optically thin and through release of the gravitational energy heated up to temperatures around 10^8 K due to shocks when the particles decelerate from supersonic speeds to subsonic speeds. These systems such as Dwarf Novae in quiescent state emit mostly hard X-rays.

If the system is in outburst state where $\dot{M}$ exceeds the $\dot{M}_{critical}$, then the boundary layer becomes optically thick due to accumulation of more particles. The boundary layer in this situation may heat up to 10^5 K temperatures due to shock. The reason that it is colder than the low $\dot{M}$ boundary layer is that cooling is more efficient since it is optically thick. Therefore mostly radiate in extreme UV or soft X-rays. (Patterson & Raymond 1985)

X-ray Spectral Properties

The spectra of the non-magnetic systems are usually described by single or two temperature bremsstrahlung model with temperatures in 1-5 keV range and absorption column N_H in the 10^{19}-10^{21} cm^{-2}. However, this approach is used mostly because of the lack of energy resolution or poor statistics of the data. As the X-ray instruments progress, the spectra become more complex. With the improvements in X-ray astronomy, it was understood that the mechanism responsible for the X-rays from CVs result from the multi-temperature thermal plasma in the boundary layer which cools from the high boundary layer temperatures to lower white dwarf surface temperatures; hence the spectra are best explained with multi-temperature plasma models (van Teeseling & Verbunt 1994, Mukai 2000, Richman H. R. 1996). The X-ray data reveals more interpretations such as multi-temperature thermal plasma emission with a flat

emission distribution indicating the radiation emission is due to cooling flow of the gas. A continuous thermal distribution and emission lines from various elements indicate the isobaric cooling flow plasma settling on the white dwarf. The initial cooling flow temperatures T_{max} are in a wide range of 8-80 keV mostly for dwarf novae (Mukai et al. 2003, Rana et al. 2006, Pandel et al 2005)).

Another characteristic of the non-magnetic CVs is that the most show line emission of Fe K_α near 6.7 keV. This emission consists of 6.4 keV fluorescent line, He-like Fe XXV line near 6.7 keV and H-like Fe XXVI line near 6.9 keV. The Fe XXV and Fe XXVI lines originate from the hot plasma with temperatures of 10^{8-9} K in the accretion disc in the shocked zones. They play important role in the diagnostics of these regions. The intensity ratio of Fe XXV and XXVI lines provides information on the ionization temperature of the plasma. Fe XXV further can be used to get information about the ionization state, temperature and density of the emitting plasma in collisional ionization equilibrium. The fluorescent line of Fe originates from the lower transitions of iron and from relatively colder plasma (less than 10^6 K). Their origin is mainly attributed to the reflection of hard rays from the surface of the white dwarf and/or inner accretion disc. In quiescent states, the main reflector is the white dwarf surface since the inner disc will be too thin. Although the line is from the reflection, the relation with the line strength and the inclination of the system is not clear yet (Rana & Singh et al. 2005).

Other than the Fe K_α complex near the 6.7 keV, other emission lines are occasionally seen in X-ray spectra, especially in data where there is enough energy resolution. Most common ones are the Fe L complex around 1 keV, and transitions of other elements such as N, O, Ne, Mg, Si and S. These emission lines provides us with better understanding of the abundance ratios, temperature distributions, electron temperatures, electron density and ionisation states of the X-ray emitting plasma. Studying the velocity broadening in the lines and looking at the velocities, one can determine the location of the X-ray emitting region whether near the fast rotating boundary layer or near the slow rotating

white dwarf. (Szkody et al. 2002, Mauche & Raymond 2000, Raymond & Brickhouse 1996)

X-ray Temporal Properties

The temporal properties depend mostly on the accretion rate of the system. Dwarf novae in quiescence (i.e. low $\dot{M}$) show different characteristics than the dwarf novae in outburst stage.

One property of X-ray light curves of the non-magnetic CVs is that in some systems orbital eclipses are detected as the X-ray emitting region is obscured. However, whether we see eclipses depends on the inclination of the system. Therefore only in systems with enough inclination angle the eclipse can be observed. Eclipses yield good diagnostics to determine the location and size of the X-ray emitting region using orbital phase and duration of ingress and egress. For dwarf novae in quiescence, X-ray eclipses are observed at the time of the optical eclipse seen. Some show, however shorter eclipse times than of the optical one. This would well mean that the X-ray emitting region is smaller than the white dwarf and close to the photosphere of the white dwarf. However, the eclipses may cease to exist during the outburst in some systems. This is explained by obscuration of boundary layer at all orbital phases. There is a case for UX UMa in outburst where the eclipse is seen only in the harder X-ray region. This accounts for the fact that the source for soft and hard X-rays have different origins. (Mukai et al. 1997, van Teeseling 1997, Ramsay et al. 2001, Wheatley & West 2003, Pratt et al. 2004)

In some observations, non-magnetic CVs also show dips in their X-ray light curves in quiescent and outburst stages. The dips are shallower in quiescent state than the outburst stage due to size of X-ray emitting region in quiescence is larger than that of the outburst while the absorbing material holds the same position. During the dips the boundary layer is obscured and hence the residual X-rays possibly come from the accretion disc corona or disc wind. The dips are attributed to interaction of the accretion stream and the disc creating cool

clouds of gas obscuring the X-rays. (Frank et al 1984, Naylor & la Dous 1997, Mason et al. 1997, Kuulkers et al. 2003))

X-ray light curves studies also show outbursts in non-magnetic CVs mostly in dwarf novae and nova-like variables. Simultaneous observations with other wavelengths such as optical and ultraviolet ranges. The X-ray outbursts lag the optical outbursts by about 12-36 hours. In the beginning of the outburst, the spectrum softens rapidly. The soft X-ray flux peaks and gradually decreases slower than the increase rate. The soft X-rays decrease and disappear before the optical outburst, hence increase and decrease times are smaller than the optical outbursts. During the increase of the soft X-rays, harder X-rays tend to be suppressed and later increases back to the quiescent levels indicating that there are two different X-ray emitting regions responsible for hard and soft X-rays. (van der Woerd et al. 1986, Wheatley et al. 2003, Mauche & Robinson 2001)

1.4.2 Polars

Origin of X-rays

In polars, due to high magnetic field strength of the white dwarf, accreting material couples on to the magnetic field lines and flows to the magnetic poles of the white dwarf. They show intensive X-ray emission, mostly soft X-rays (about 10^{32} ergs/s), some hard X-rays depending on the accretion rate. They also show cyclotron emission at longer wavelengths from IR to UV. (Mukai 2003, Kuulkers et. al. 2006)

According to the standard model accreting material falling on to the white dwarf almost vertically forms a strong stand-off shock close to the surface due to high speed of the accretion material. Most of the radiation at all wavelengths including hard X-rays originate in this shock region when the material is heated up to 10-40 keV energies due to the shock and cooled as material settles on the white dwarf. The soft X-rays with temperatures of (10^5 K) arise from the

absorbed and re-radiated emission from the footprints of the accretion column surrounding the area of hard X-ray emitting region (Wu 2000, King & Lasota 1979, Lamb & Masters 1979).

Early X-ray observations with ROSAT pointed out that the soft X-ray emission is much higher than the expected as in the standard model. This was explained by assuming that the accretion is in forms of blobs rather than uniform streams penetrate into the photosphere. The shock region is then buried and hard X-rays are thermalised releasing soft X-rays. Late observations with XMM-Newton shows that the excess is not as much as the ROSAT data presents. Moreover, XMM-Newton data established that low accretion systems ($\dot{M} < 10^{-11}\mathrm{M}_{\odot}\ \mathrm{yr}^{-1}$) show very little soft components than the high accretion systems. (Ramsay et al. 1994, Ramsay & Cropper 2004, Ramsay et al. 2004)

X-ray Spectral Properties

As in the case of non-magnetic systems, early low signal-to-noise, low resolution spectral data of polars were fit with simple bremsstrahlung model with temperatures about 15 keV with a simpler absorber and a reflection coefficient to account for the reflected emission from the surface of the white dwarf. Later, with better spectral data, the main approach was using bremsstrahlung component for the hard X-rays and blackbody component for the soft X-rays (Ramsay et al. 1994, Beuermann & Burwitz 1995, (Mukai 2003)). The soft component spectrum should be more complicated however mostly blackbody is used for simplicity. For the hard X-ray emission, since the accreted matter cools from high temperature in the shock front to lower temperatures at the bottom of the shock region, multi-temperature shock models were established (Cropper et. al 2000). Multi-temperature plasma models such as MEKAL with various temperatures or plasma emission with continuous emission measure (CEVMEKL) were also used to fit the hard X-ray spectra from polars. (Singh et al. 2004, Schwarz et al 2005)

Line emission is also observed in polars, since recent X-ray missions have can

resolve them. The most common one is (although not many polars show strong intensities) the Fe K_α complex near the 6.7 keV as with non-magnetic CVs. The K_α complex is comprised of He-like, H-like and fluorescent Fe emission lines produced in the post-shock region where the multi-temperature plasma is present. The line complex is a good tool for determination of white dwarf mass and for density diagnostics. They show low doppler shifts meaning the emission is from the lower and denser base of the accretion column. The line profiles are affected from the cyclotron cooling and compton scattering effects. Spin modulation of the width of the lines were also reported. (Hellier & Mukai 2004, Terada et al. 2004, McNamara et al. 2007)

X-ray Temporal Properties

Although simple accretion geometry, polars display a rich phenomenology of X-ray light curves. X-ray light curve modulation has many aspects such as the locations of the accretion spots, stellar eclipses, changes in the accretion and absorption within the system. In long terms, the light curves are affected by the shifts of locations of the accretion region, changes of from one-pole to -two pole accretion and large variations in $\dot{M}$ which is attributed to the star spots on the secondary at L_1 (Kuulkers et al 2006).

The X-ray light curve of one pole accreting polar has five distinct characteristics which is demonstrated in Figure 1.8. Firstly, there is a clear on-off pattern caused by the occultation of the accretion spot by the white dwarf which does not totally obliterate the X-rays, however reduces the count rate by a great deal (In Figure 1.8 region a). Second, total eclipse of the secondary star which happens at a different phase than the eclipse of the white dwarf (In Figure 1.8 region b). Then there is a narrow dip caused by obscuration by the accretion stream (In Figure 1.8 region c). There is also an absorption from the accretion curtain that reduces the X-ray count rate (In Figure 1.8 region d). Lastly there is a broad dip caused by the absorption or scattering of photons in the accretion column just above the accretion spot (In Figure 1.8 region e). (Schwope et al.

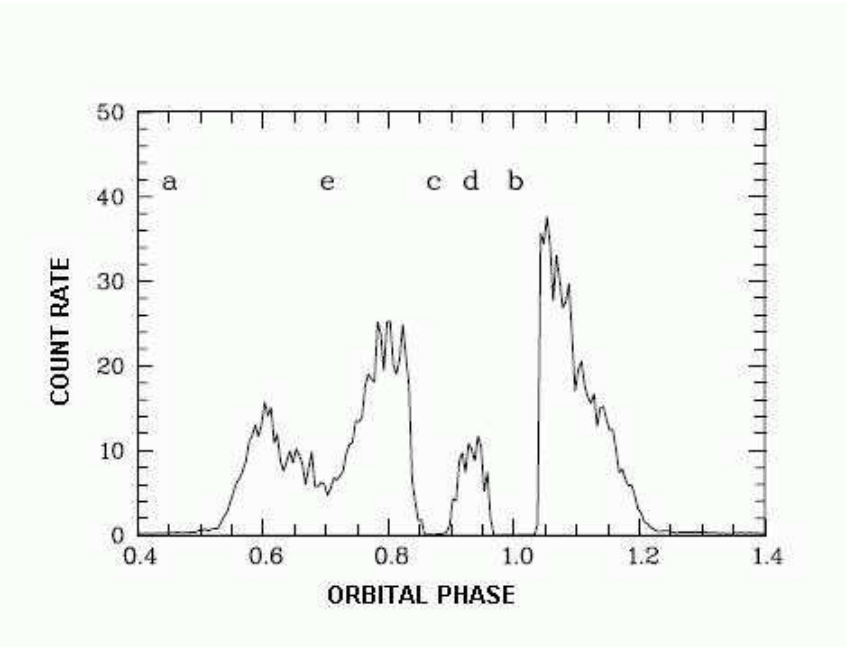

Figure 1.8: ROSAT X-ray Light Curve of the Polar HU Aqr

(Region a corresponds to the occultation of the X-ray source by the white dwarf, region b corresponds to eclipse by the secondary, region c is the narrow dip, region d correspond to absorption by the accretion column and region e correspond to the broad dip. Adapted from Schwope et al. (2001))

2001, Ramsay et al. 2004)

For polars with low accretion rate the X-ray light curve may not show modulation although modulations are seen in optical light curves. This is because the low count rates in X-rays and possibly the X-ray source being the corona of the secondary rather than accretion (Szkody et al. 2004)

1.4.3 Intermediate Polars

Origin of X-rays

In intermediate polars the matter from the donor accretes on the white dwarf on the magnetic poles as in polars. However, due to their low magnetic field strengths a truncated accretion disc may exist in intermediate polars, also their accretion region is more extended than polars. They are the most luminous hard X-ray (2-10 keV) emitters among CVs with luminosities in the order of 10^{33} erg/s and show weak or no cyclotron emissions (Mukai 2003).

Although intermediate polars have smaller magnetic fields and have different accretion geometries than polars, their X-ray production processes are mostly similar. The magnetically channeled accretion material reaches very high speeds up to 3000-10000 km/s forming a shock region near the surface of the white dwarf where the material has temperatures higher than 10^8 K. The accreting material then settles on to the white dwarf emitting hard X-rays. (Patterson 1994)

Early work suggested that intermediate polars lack soft X-ray emissions in contrast to polars. The reason was thought to be higher absorption due to larger accretion area, higher accretion rate or lower white dwarf mass than the polars (King & Lasota 1990). However later observations proved some IPs to have soft X-ray components due to reprocessing of hard X-rays by the surface of the white dwarf (not because of the blobby accretion as suggested for some polars) , and reason for the lack of soft X-rays from some IPs was pointed out as the geometrical properties: obscuration by the accretion curtain (Evans &

Hellier 2007)

X-ray Spectral Properties

As in the general case for CVs, early low signal-to-noise data fitted with single temperature (however with higher temperatures in orders of 10 keV) bremsstrahlung along with a partial absorber varying with phase (Norton & Watson 1989). The approach was further advanced with multi-temperature emission models including reflection effects and partially ionized absorbers which enabled the determination of the white dwarf mass. (Cropper et al. 1998)

Recent observations indicating soft X-ray component of the spectra resulting from the irradiation of the white dwarf around the accretion curtain lead to including soft blackbody emission with temperatures around several 10s of eVs. Commonly used recent fitting models combines multi-temperature optically thin plasma along with a soft blackbody component and partially covering absorber which takes into account the multi-temperature nature of the hard X-ray emission from the post-shock region, soft X-ray emission and absorption due to the accretion region(Evans et al. 2006, de Martino et al. 2006). A different approach requires photoionized plasma model which has a hard power law-like continuum and line emissions from medium elements for spectral fitting (Mukai et al. 2003).

Line emissions from various elements contribute highly to the spectrum of IPs. Various emission lines from O, Ne, Mg, Si, S, and Fe were detected in IPs as an evidence for the multi-temperature plasma in the shock region. The line ratios proves a basis for constraining the temperature at the shock region and white dwarf mass as well as elemental abundances (Fujimoto & Ishida 1997, Mukai et al. 2001, Mukai et al. 2003). Fe K_α complex also plays an important part in the spectra. Apart from the iron abundance, Fe K_α line ratios is a tool for the diagnostics for the ionization temperatures in the post-shock plasma. Doppler shifts in these lines give account for the X-ray emitting region. Fe fluorescent line at 6.4 keV relates to the irradiation of the surface of the white

dwarf and hence provides information on the accretion column (Hellier & Mukai 2004, Ezuka & Ishida 1999).

X-ray Temporal Properties

The main characteristic of intermediate polars distinguishing them from the polars is that due to less magnetic field strength, the white dwarf spin is not synchronized with the orbital period. In fact the spin period is much less than the orbital period in these systems. Thus two different periodicities are detected in power spectra of the IPs which is an essential criterion for the classification of a system as an IP. There is also a plausible relation between two periodicities as P_{spin}/P_{orb} usually around 0.1 or less (Norton et al. 2004).

Basically X-ray light curves folded on the spin period of the white dwarf shows sinusoidal behavior in phase with the optical. The X-ray modulation of the spin period was attributed to the absorption by the accretion column (Hellier et al. 1991). However, later observations indicated that in some IPs the pulse profile show more complex properties such as double peak pulses, saw tooth shape pulses, changing profiles with energy and changes in profiles during outbursts. One is the double peak behavior attributed to short P_{spin} systems where the magnetic field is weak. Due to weak magnetic field the accretion curtain footprints are wide and the optical depths to X-ray emission within the accretion curtains are therefore lowest in the direction along the magnetic field lines and highest in the direction parallel to the white dwarf surface, such that the emission from the two poles conspires to produce double-peaked X-ray pulse profile. The sawtooth profile is explained by the offset of the magnetic axis from the white dwarf center. The energy dependent spin period modulation is explained by a partially covered absorber system, with a small change in the covering fraction being sufficient to explain the in-phase soft X-ray modulation without affecting the harder X-rays. The change of profiles during outbursts is explained by the disc being pushed inward during the outburst blocking the view to the lower accretion pole and causing larger pulsation during the outburst

(Norton et al. 1999, Hellier et al. 1997, Rana et al. 2004, Evans & Hellier 2004,).

Other features seen in X-ray light curves are the eclipses resembling dips in LMXBs over the orbital period related to the photoelectric absorption, and sideband period ((P_{spin}^{-1} - P_{orb}^{-1})$^{-1}$) modulation in slow rotating systems with high magnetic fields as an indication of discless accretion. (Hellier et al. 1993, Buckley et al. 1997, Hellier & Beardmore 2002)

CHAPTER 2

OBSERVATION AND DATA

2.1 The Source

Classical nova RR Pic had an outburst in 1925 as a slow nova (expansion speed $\sim$ 400 km/s). The shell shows "equatorial ring and polar cap/blob" geometry. There are similarities and important differences between the spectra in the ring and blob regions (in C and O lines) with a shell size of 30″x21″ and expansion rate of 850 km/s for the ring (Gill & O'Brien 1998). The distance of the nova is measured to be 600±60 pc (Gill & O'Brien 1998).

The point source RR Pic has an orbital period of $P_{orb}\sim 0.^{d}145025$ (Vogt 1975). A different periodicity of 15 min is detected by Kubiak (1984) and accounted for the white dwarf period; hence making the source a candidate for intermediate polars. However, Haefner and Schoembs (1985) couldn't find the 15 min period with high-resolution photometry and concluded that the 15 min period is a transient event in the disc rather than the period of the white dwarf. Warner (1986) also confirms the absence of this 15 min period. Additionally he also finds flickering activity independent of the orbital phase coming from the disc itself rather than the hotspot and the system. Another period of 0.1577 days has also been found which was interpreted as the superhump period of the system (Schmidtobreick et al. 2006). According to its eclipse properties, the system's orbital inclination angle was constrained to be in an interval between 60^{o} and 80^{o} (Ribeiro & Diaz 2006).

Furthermore, the source has a hardness ratio similar to Polars and the source spectrum in general differs compared with the non-magnetic CVs (van Teeseling et al. 1996) which indicates the existence of soft excess in the system. In addition, polarization measurements indicate the existence of two components of emission, one in the inner disk and the other associated with a hot spot in the disk (Haefner & Metz 1982).

2.2 Observation and Data Preparation

RR Pic and its vicinity was observed using the CHANDRA (Weisskopf, O'dell & van Speybroeck) Advanced CCD Imaging Spectrometer (ACIS; Garmire et al. 1992) for a 25 ksec on 2001 October 30, pointed at the nominal point on S3 (the back-illuminated CCD) with no gratings in use yielding a moderate non-dispersive energy resolution. The data were obtained at the FAINT mode. CHANDRA has two focal-plane cameras and two sets of transmission gratings that can be inserted in the optical path (HETG and LETG; High and Low Energy Transmission Gratings). The ACIS is used either to take high resolution images with moderate spectral resolution or is used as a read out device for the transmission gratings. ACIS is comprised of two CCD arrays, a 4-chip array, ACIS-I; and a 6-chip array, ACIS-S. The ACIS-S3 has a moderate spectral resolution $E/\Delta E \sim$ 10-30 (falls to about 7 below 1 keV) with an unprecedented angular resolution of $0.49''$ per pixel (half-power diameter). The standard pipeline processing of the event files was done by CXC.

For the spectral and temporal analysis of the data we did ACIS process events using CIAO 3.2 (Fruscione & Siemiginowska 2000), XSPEC 11.3.1 (Arnaud 1996) and XRONOS 5.21 (Stella & Angelini 1992). For spectral analysis, first using the "psextract" script we extracted the source and background spectra and create Response Matrix File (RMF) and Ancillary Response File (ARF). Then we binned the spectrum such that each bin contains data with signal-to-noise ratio higher than 3 using "dmgroup". The data was then plotted using

XSPEC and fitted with models existing in XSPEC. Data points below 0.3 keV and above 5.0 were omitted since these data points were statistically insignificant. For the timing analysis, we extracted the background subtracted light curve of the source using "dmextract". After applying barycentric correction using "axbary" in CIAO, the light curve was rebinned and plotted by using "lcurve" task in XRONOS. The light curve was then folded and plotted by the "efold" task. For the phase binned spectroscopy, spectra with the appropriate phases were extracted using "dmextract" and "dmtcalc" and fitted to models using XSPEC software.

CHAPTER 3

RESULTS

3.1 The CHANDRA Spectrum of the Point Source

After the extraction and binning, the source spectrum was fitted with various models using the XSPEC software.

The CHANDRA spectrum of the source can not be fitted by a single or two-temperature bremsstrahlung model including photoelectric absorption (*phabs*, *wabs* (models in XSPEC)) with reduced χ^2 values smaller than 2. A fit with a single bremsstrahlung model is presented in Figure 3.1. The fit doesn't actually reflect the features of the spectrum properly leaving a hard excess above 2 keV. Moreover, the residuals of the fit in Figure 3.1 are scattered around the mean up to 4σ levels in the 0.5-2 keV region. To reduce the scattering of the residuals we added two absorption lines to the bremsstrahlung around 1.15 keV and 1.25 keV which improved the fit diminishing the reduced χ^2 down to 1.75 but still maintaining the scattering around 0.5-1 keV and the hard excess (See Figure 3.2). Thus, we concluded that there are line contributions to the continuum in the 0.5-1 keV region. Including emission lines to the fit both reduced the hard excess and the scattering of the data as well as improving the reduced χ^2 to 1.13.

Therefore the most proper fit is with a composite model of Bremsstrahlung together with a simple photoelectric absorption of HI, two absorption lines around 1.1-1.4 keV and 5 Gaussians centered on the likely emission lines around

Table 3.1: Spectral parameters of the entire spectrum of the RR Pic in the energy range 0.3-5 keV.

	BREMSS+2ABS+5GAUSS	BREMSS+BBODY	BBODY+CEVMKL
N_H (10^{22} atoms/cm^2)	$0.008^{+0.014}_{-0.008}$	$0.40^{+0.17}_{-0.12}$	$0.21^{+0.13}_{-0.21}$
kT_{Bremss} (keV)	$1.33^{+0.27}_{-0.34}$	$0.2^{+0.01}_{-0.03}$	N/A
kT_{BB} (keV)	N/A	$0.66^{+0.17}_{-0.11}$	$0.13^{+0.03}_{-0.04}$
T_{max} (keV)	N/A	N/A	$8.1^{+11.9}_{-3.8}$
K_{Bremss}	$0.000087^{+0.000025}_{-0.000020}$	$0.015^{+0.035}_{-0.003}$	N/A
K_{BB}	N/A	$0.000001^{+0.0000002}_{-0.0000002}$	$0.0000084^{+0.000048}_{-0.0000042}$
K_{CEVMKL}	N/A	N/A	$0.0002^{+0.00005}_{-0.00005}$
Gabs LineE (keV)	A1: $1.14^{+0.03}_{-0.02}$	N/A	N/A
	A2: $1.28^{+0.02}_{-0.02}$		
Gaussian LineE (keV)	G1: $0.526^{+0.052}_{-0.086}$	N/A	N/A
	G2: $0.664^{+0.035}_{-0.024}$		
	G3: $0.799^{+0.018}_{-0.019}$		
	G4: $0.900^{+0.019}_{-0.020}$		
	G5: $1.02^{+0.02}_{-0.02}$		
K_G	G1: $0.0000073^{+0.0000044}_{-0.0000051}$	N/A	N/A
	G2: $0.0000094^{+0.0000041}_{-0.0000041}$		
	G3: $0.000014^{+0.000002}_{-0.000004}$		
	G4: $0.0000084^{+0.0000028}_{-0.0000024}$		
	G5: $0.0000062^{+0.0000019}_{-0.000002}$		
Flux (10^{-13} ergs/cm^2/s)	$2.51^{+0.39}_{-1.21}$	$0.52^{+0.2}_{-0.18}$	$0.87^{+0.19}_{-0.85}$
	Bremss: $0.4^{+0.46}_{-0.28}$	Bremss : $0.008^{+0.11}_{-0.008}$	CEVMKL: $0.87^{+0.16}_{-0.14}$
	G1: $0.065^{+0.095}_{-0.064}$	BBODY: $0.51^{+0.1}_{-0.13}$	BBODY: $0.00097^{+0.00095}_{-0.00048}$
	G2: $0.11^{+0.08}_{-0.09}$		
	G3: $0.19^{+0.06}_{-0.19}$		
	G4: $0.13^{+0.08}_{-0.07}$		
	G5: $0.11^{+0.1}_{-0.08}$		
χ^2_ν	1.13 (73 d.o.f.)	1.50 (79 d.o.f.)	1.30 (78 d.o.f.)

(N_H is the absorbing column, kT_{Bremss} and kT_{BB} are bremsstrahlung and blackbody temperatures respectively, T_{max} is the maximum temperature for CEVMKL model, Gabs LineE is the absorption line centers for the absorption lines, (the sigma and Tau parameters are frozen at 0.005 and 50 for the first line and 0.01 and 20 for the second line), Gaussian LineE is the line center for the emission lines (the sigma values for the lines are frozen at 0.001); K_{Bremss}, K_{BB}, K_{CEVMKL}, K_G are the normalizations for bremsstrahlung, blackbody, CEVMKL and Gaussian models respectively. The fluxes are given for the entire model in the first row and then for each of the components in the following rows. All error ranges are given in %90 confidence level ($\Delta\chi^2$=2.71 for a single parameter)

0.3-1.1 keV energies. The fit is shown in Figure 3.3 and model parameters are listed in Table 3.1. The Gaussian lines fitted in the model correspond to a range of emission lines of Fe (transitions between XVII and XXIV), S (XIV and XVI), Ca (transitions between XV and XVII), Ne (IX, X), O (VII, VIII), C VI; the absorption lines correspond to Fe (transitions between XVII and XXIV), Ne (X, IX) and Na X. However, due the spectral resolution limitations of ACIS-S, the exact emission lines and absorption lines with correct ionization levels cannot be determined.

According to van Teeseling et. al (1996), along with a model that describes the photoelectric absorption of neutral H in the line of sight a composite model of blackbody plus a bremsstrahlung also fits the spectrum. So we applied a fit with a composite model of a bremsstrahlung yielding a temperature of 0.2 keV plus a blackbody yielding a temperature of 0.66 keV along with an N_H; neutral column density of H (See Figure 3.4 for the fit and Table 3.1 for the parameters). The fit has a reduced χ^2 of 1.5, however, the model leads to a soft excess in the spectrum and the absorption and emission features visible in the spectrum are not truly reflected.

The spectrum could be fit with models like CEVMKL (Singh et al. 1996) that includes a power law of temperature distribution as well as emission measures. The fit shows a reduced χ^2 value greater than 2 and excess at the hard and soft ends of the spectrum. The hard excess could be lifted by adding a blackbody component to the model with temperature around 0.13 keV. (See Table 3.1) therefore improving the χ^2 value to 1.30. However the soft excess is still persistent in this composite model. (See Figure 3.5)

The hard excess part of the spectrum is best fitted with a cooling flow model such as VMCFLOW (Mushotzky & Szymkowiak 1988) but below 1.0 keV the model does not yield the desired fit values therefore results in a χ^2 value higher than 2 (See Figure 3.6). Changing the elemental abundances of O, Ne, Na and Fe does not improve the fit. The only way to decrease the reduced χ^2 value below 2 is to add a blackbody component with a temperature of 0.42 keV.

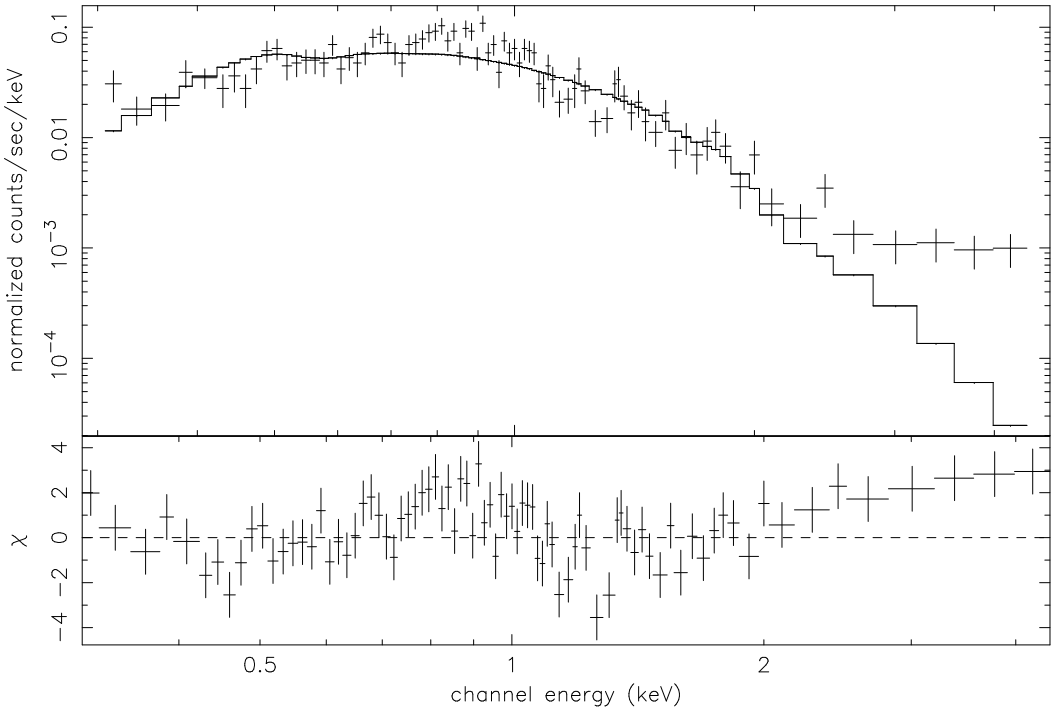

Figure 3.1: The Spectrum Fitted with Simple Bremsstrahlung

(The crosses show the data with error bars and solid line show the fitted model. The panel under the spectrum shows residuals in standard deviations.)

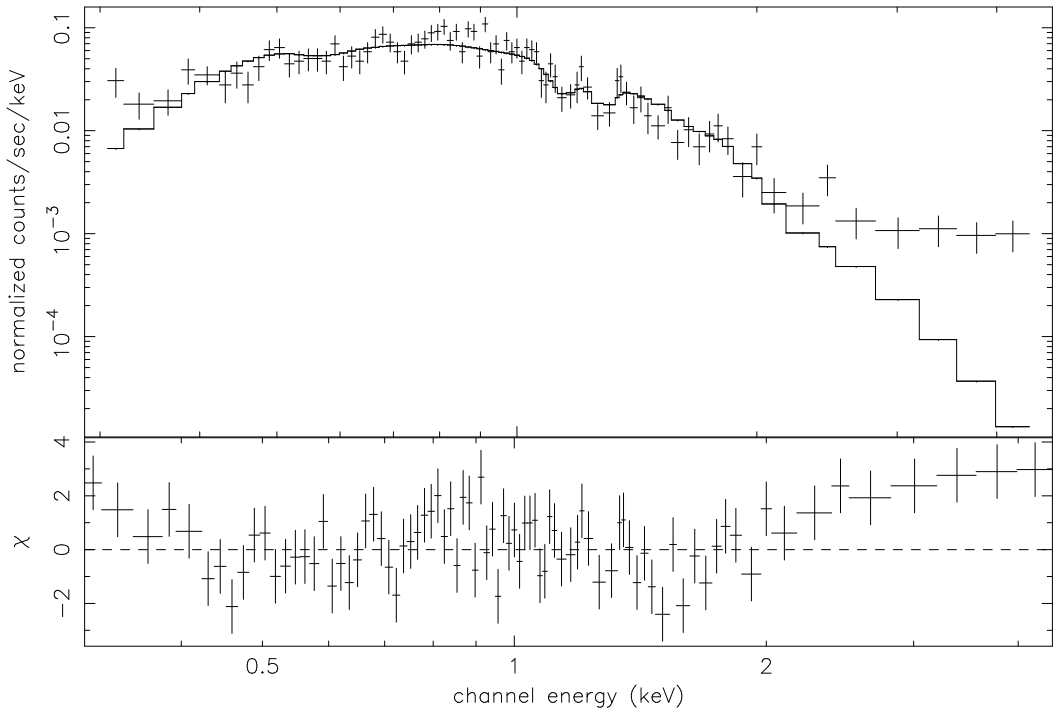

Figure 3.2: The Spectrum Fitted with Bremsstrahlung and two Absorption Lines (GABS)

(The crosses show the data with error bars and solid line shows the composite fitted model. The panel under the spectrum shows residuals in standard deviations.)

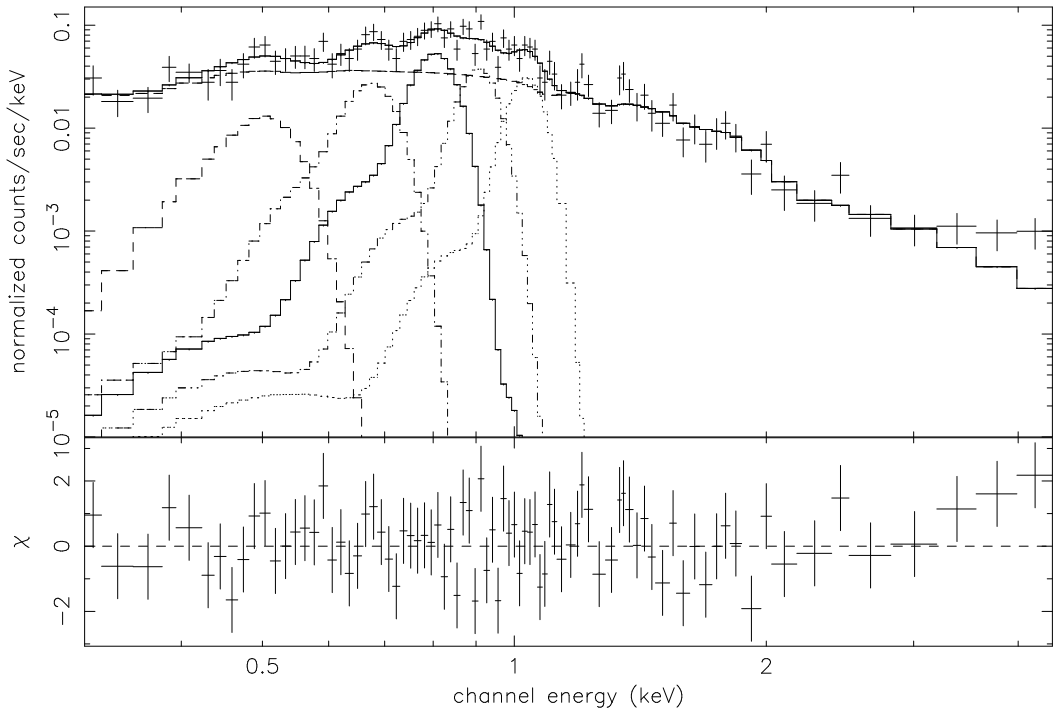

Figure 3.3: The Spectrum Fitted Bremsstrahlung with two Absorption Lines (GABS) and five Emission Lines (GAUSS)

(The crosses show the data with error bars, solid line shows the composite fitted model and the dashed/dotted lines show the individual models. The panel under the spectrum shows residuals in standard deviations.)

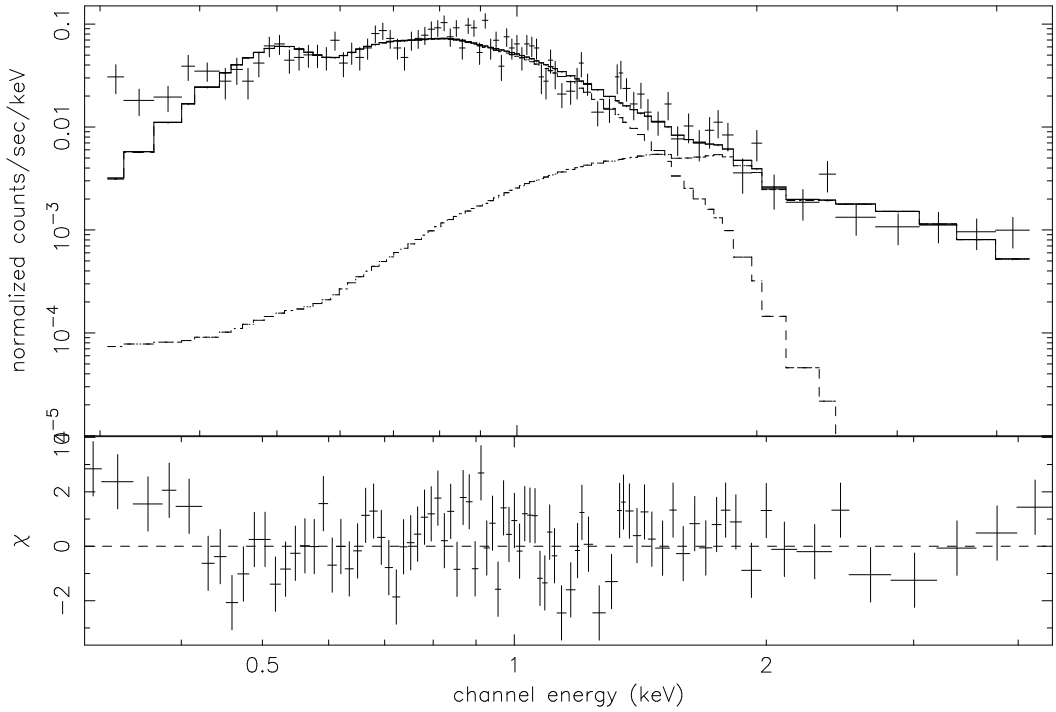

Figure 3.4: The Spectrum Fitted with a (Bremsstrahlung + Blackbody) Model

(The crosses show the data with error bars, solid line shows the composite fitted model and the dashed/dotted lines show the individual models. The panel under the spectrum shows residuals in standard deviations.)

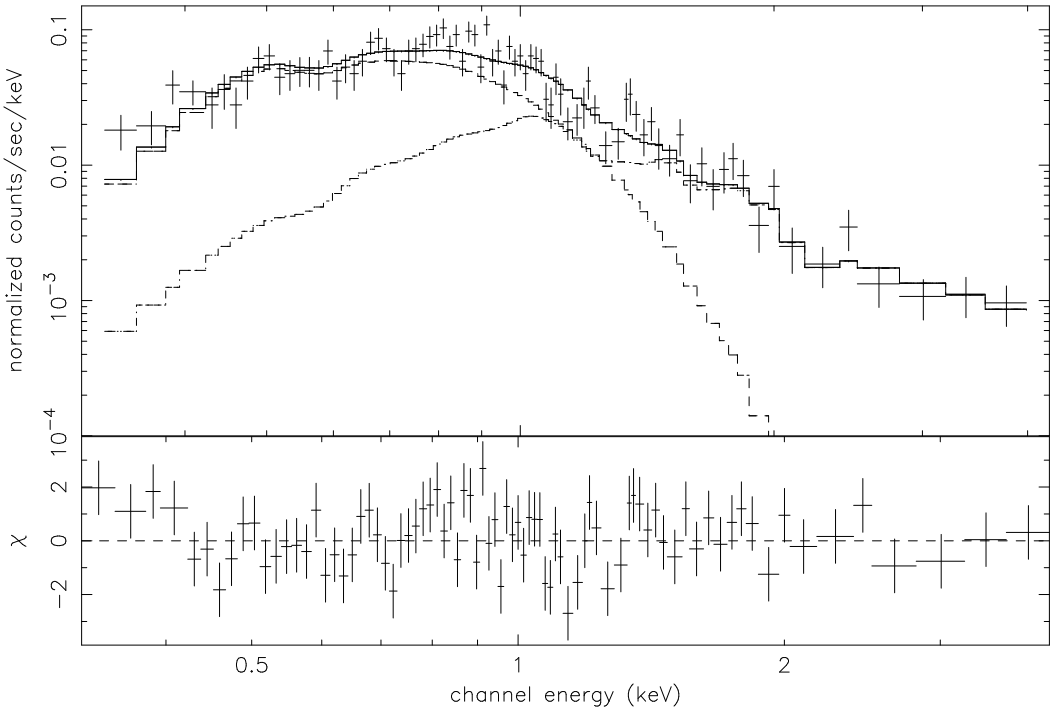

Figure 3.5: The Spectrum Fitted with a (CEVMKL + Blackbody) Model

(The crosses show the data with error bars, solid line shows the composite fitted model and the dashed/dotted lines show the individual models. The panel under the spectrum shows residuals in standard deviations.)

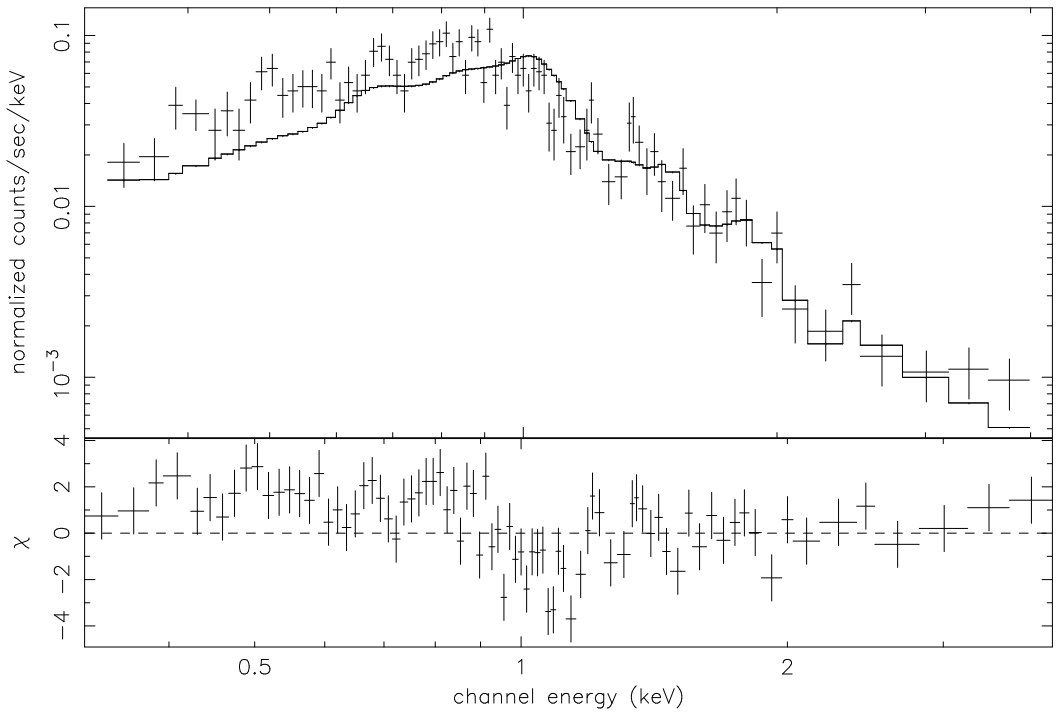

Figure 3.6: The Spectrum Fitted with VMCFLOW

(The crosses show the data with error bars and solid line show the fitted model. The panel under the spectrum shows residuals in standard deviations)

3.2 Temporal Analysis of the Point Source

The background subtracted light curve extraction of the source was done by the standard CIAO ACIS light curve extraction procedures. Plotting and epoch folding were performed with XRONOS 5.21.

Figure 3.7 shows background subtracted time series with bin time of 1100 s. The X-ray light curve of the source shows variation when folded on the orbital period of the system, 12530 s (0.14502545 d) which is shown in Figure 3.8. The light curve in Figure 3.7 has been used for the folding process. We used the epoch as the start time of the observation made by Schmidtobreick et al. (2003) for radial velocities curve (HJD = 2452328.578335). So the ephemeris of the zero point of the radial velocity curve is 2452328.578335 + 0.14502545(7)E where E is the number of cycles. We calculated error in our phase as 0.00004 phases using the equation

$$\Delta_{phase} = \frac{JD_{obs} - JD_{epoch}}{P_{orb}^2}\Delta_{orb} \tag{3.1}$$

where Δ_{phase} is the error in the phase, JD_{obs} is the start time of our observation (2452212.599797), JD_{epoch} is epoch in our folded light curve (2452328.578335), P_{orb} is the orbital period 0.14502545 days and Δ_{orb} is the error of the orbital period 0.000000007 days.

We did another folded light curve (Figure 3.9), this time using the eclipse time of Warner's light curve S3464 from December 1984 (Warner 1986) as our epoch (HJD=2446064.441). The aim was to phase-lock the X-ray light curve to the optical light curve of Warner. The ephemeris of the eclipse is 2446064.441 + 0.14502545(7)E where E is the number of cycles. The error in the phase using Equation 3.1 is found as 0.002 phases.

A simple sinusoidal fit to the folded light curve in Figure 3.8 yields an X-ray modulation amplitude of 0.02 counts/s with 30% statistical error (Figure 3.10).

We also performed orbital phase resolved spectroscopy of the source by extracting phases between 0-0.2 for the maxima and 0.3-0.45 for the minima in

Table 3.2: Spectral parameters of maximum and minimum spectra in the 0.3-5 keV region.

	Maxima	Minima
N_H (10^{22} atoms/cm^2)	$0.25^{+0.23}_{-0.18}$	$0.64^{+0.14}_{-0.13}$
kT$_{Bremss}$ (keV)	$0.35^{+0.2}_{-0.13}$	$0.14^{+0.21}_{-0.04}$
K$_{Bremss}$	$0.0004^{+0.0028}_{<}$	$0.03^{>}_{-0.03}$
χ^2_ν	1.05 (15 d.o.f.)	0.49 (6 d.o.f.)

Both spectra were fit with a bremsstrahlung and photoelectric absorption. N_H is the absorbing column, kT_{Bremss} is the bremsstrahlung temperature and K_{Bremss} is the bremsstrahlung normalization. Error ranges for kT_{Bremss} and K_{Bremss} correspond to 2σ confidence level, error range for N_H correspond to 3σ confidence level.

Figure 3.8. Figure 3.11 shows the fit to the maximum spectrum and Figure 3.12 the minimum spectrum using a model with a single bremsstrahlung along with photoelectric absorption. The gaussian absorption and emission lines used in the entire spectrum were not used in these spectra. This was due to the low statistical quality of the minimum and maximum phase spectra which does not allow the detection of lines. The fit parameters are given in Table 3.2. The fits show a difference in neutral Hydrogen absorption between minimum and maximum spectrum in the 3σ confidence range.

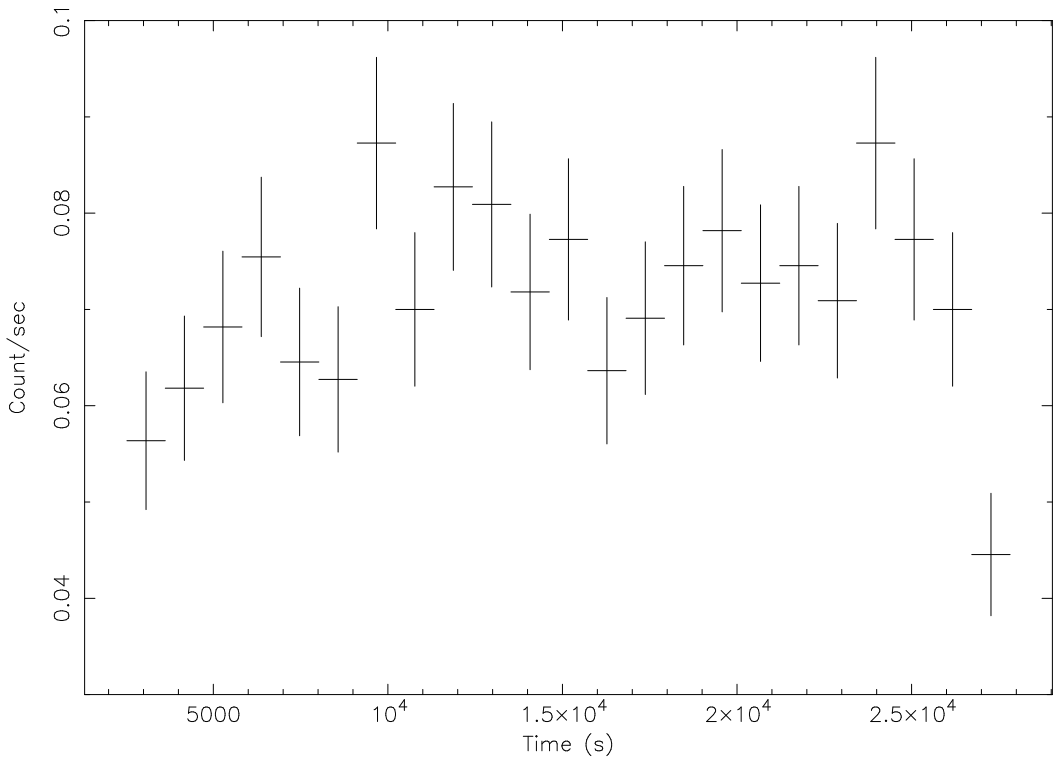

Figure 3.7: The X-ray Light Curve of RR Pic

(The light curve was binned with 1100 seconds.)

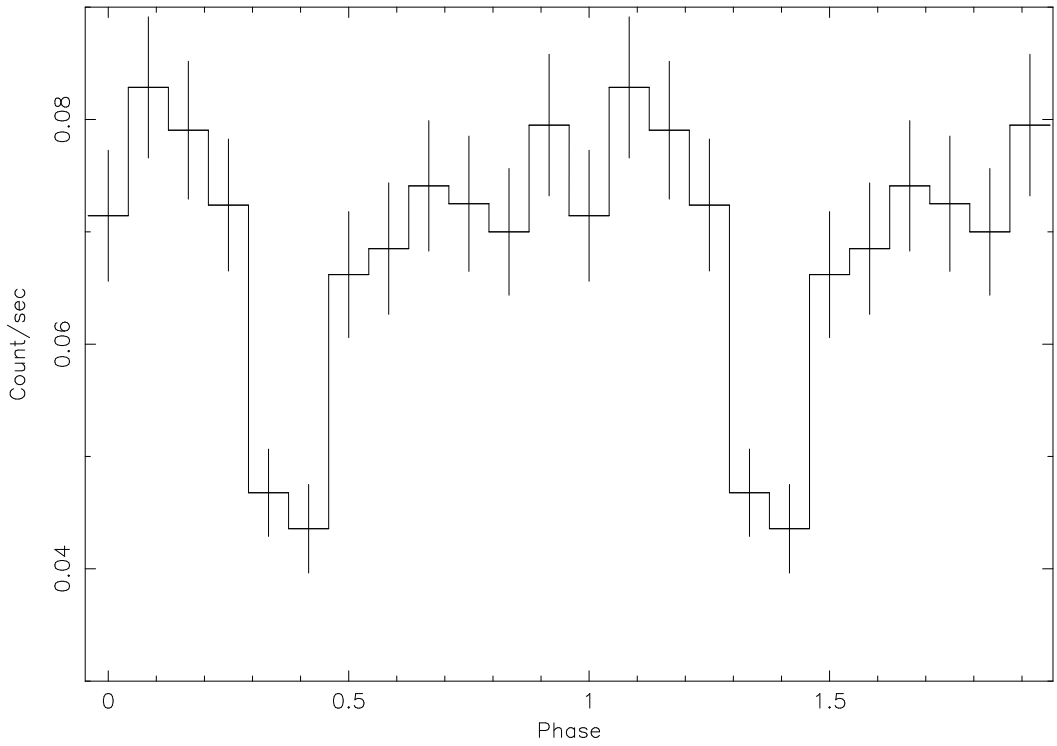

Figure 3.8: The Folded Light Curve of RR Pic

(The light curve in Figure 3.7 was used and folded over the orbital period which is 0.14502545 days. The epoch is HJD = 2452328.578335)

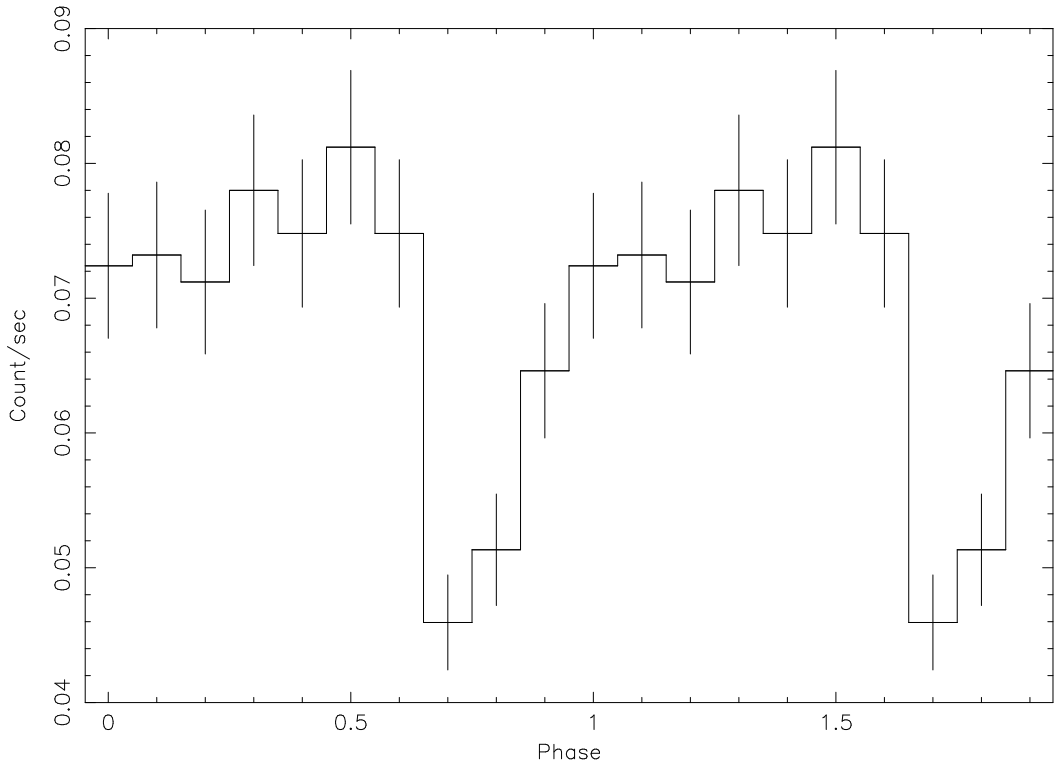

Figure 3.9: The Folded Light Curve of RR Pic

(The light curve in Figure 3.7 was used and folded over the orbital period which is 0.145025 days. The epoch is HJD = 2446064.441)

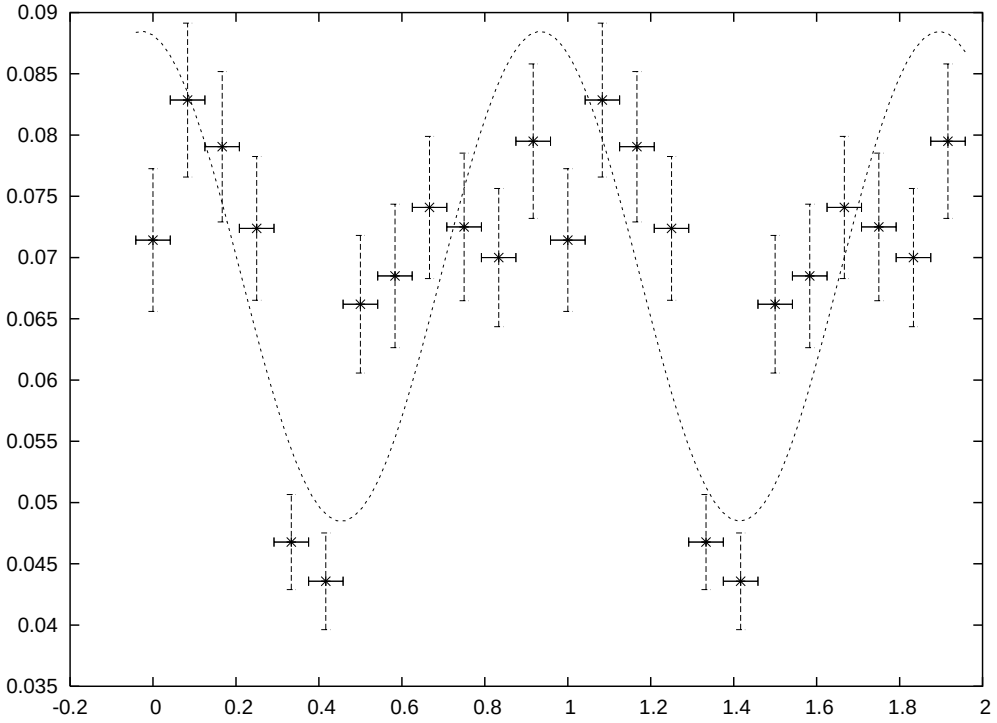

Figure 3.10: Simple Sine Function Fitted To the Folded Light Curve

(The crosses show the folded light curve data and dashed line shows the fitted sine function)

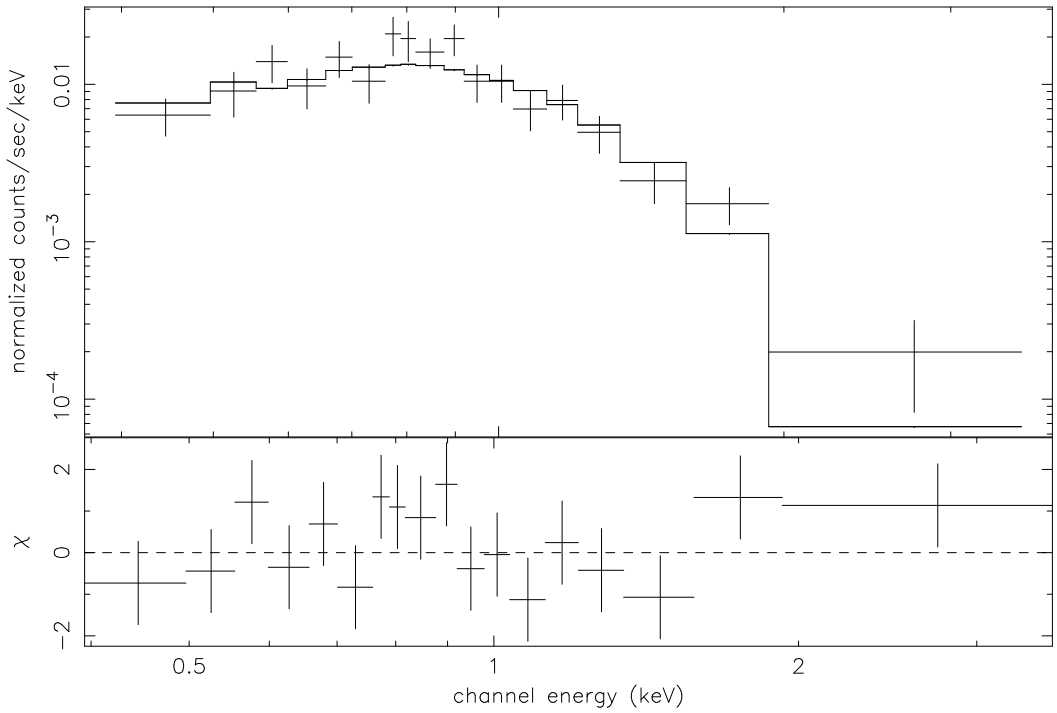

Figure 3.11: The Spectrum of the Maximum Phase

(The spectrum was fitted with a bremsstrahlung times a photoelectric absorption of HI. The crosses show the data with error bars and solid line shows the composite fitted model. The panel under the spectrum shows residuals in standard deviations.)

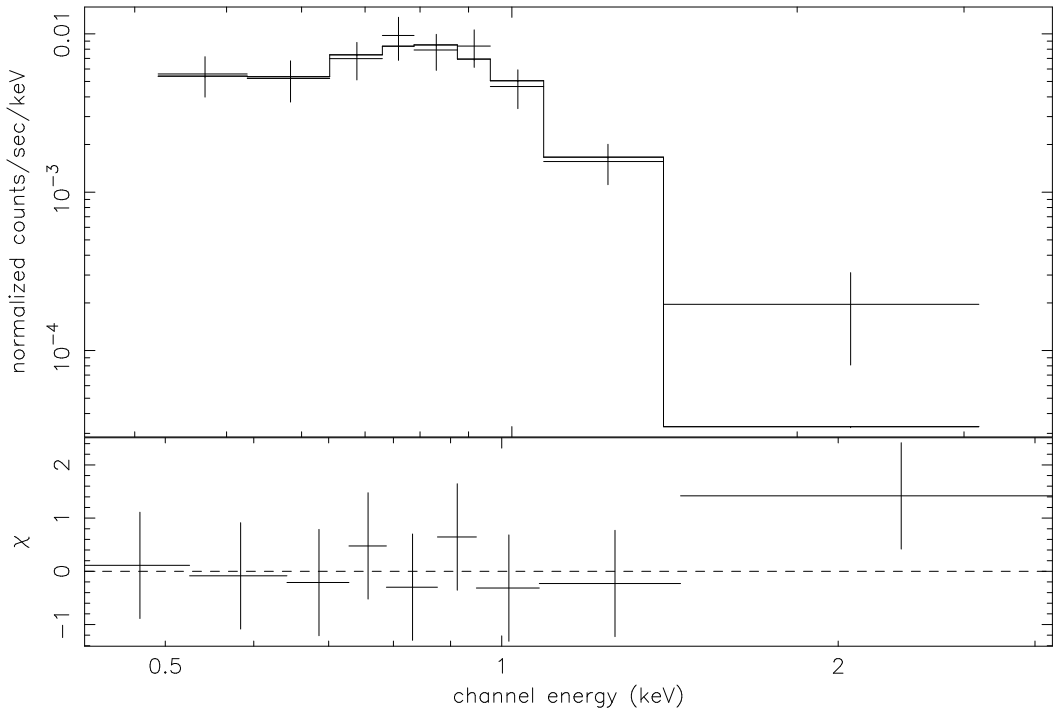

Figure 3.12: The Spectrum of the Minimum Phase

(The spectrum was fitted with a bremsstrahlung times a photoelectric absorption of HI. The crosses show the data with error bars and solid line shows the composite fitted model. The panel under the spectrum shows residuals in standard deviations.)

CHAPTER 4

DISCUSSION

The CHANDRA ACIS-S spectrum of RR Pic best fits with a composite model of single bremsstrahlung, photoelectric absorption, two absorption lines and 5 Gaussian lines. The detection of lines are at 2-3σ confidence level.

According to Mukai et al. (2003) X-ray spectra of CVs can be categorized into two; one being the cooling flow model and the other one photoionized plasma model. RR Pic spectrum shows similar characteristics with V1223, AO Psc and GK Per (which were classified by Mukai et al. (2003) as photoionized plasma) which show emission lines of Fe XVII, O VII, O VIII, Ne X and Ne IX. Further, our spectrum does not fit with a cooling flow model (VMCFLOW). This comparison of fitted models may imply that the X-ray source is a photoionized plasma rather than cooling flow gas. However, this conclusion may not be definitive since the data Mukai et al. (2003) fitted the models were obtained using high-energy transmission grating (HETG) with the resolving power of $E/\Delta E \sim$ 1070-65 which is much higher than ACIS-S. Hence spectral resolution of our data is rather poor and the emission lines are not clearly resolved.

Adding a blackbody component to the bremsstrahlung model as suggested by van Teeseling et. al. (1996) improves the fit; however the blackbody temperature of the fit is in the 0.55-0.83 keV range which is too high for any physical interpretation. The same conditions hold for CEVMKL plus a blackbody model. Although the fit is acceptable, the blackbody temperature which should be in the order of 10 eV (e.g. Evans & Hellier 2007) is also too high to have any

physical meaning. Hence no decisive physical conclusions can be made with these models.

The two absorption lines detected in the spectrum around 1.1-1.2 keV were not discovered before in any CV. The first absorption line correspond to Fe (transitions between XVII and XXII), the second one correspond to Fe (transitions between XIV and XXVI). The absorption lines are not due to the contamination of the CHANDRA such as the iridium and carbon edge.

The light curve of the source shows variation folded on the orbital period with a modulation amplitude of 0.02 counts/s with a statistical error of 30%. Comparing the spectra of orbital maximum and minimum of the source reveals that the X-ray modulation could be due to the difference in photoelectric absorption between the two phases. This feature along with the classification of the source spectrum as a photoionized spectrum which Mukai et al. (2003) found belonging to intermediate polars may imply the idea that the source can be an intermediate polar. The increase of the photoelectric absorption during the orbital minimum can be due to the obscuration by the accretion curtain of the white dwarf (Kuulkers et al. 2003). However, this would imply that the period observed is the white dwarf spin period rather than the orbital period of the system. To overcome this contradiction, analogy to the Low Mass X-ray Binaries (LMXBs) can be used. In LMXBs, the X-ray intensity shows dips caused by the obscuration of the X-rays by the region where the accretion material impacts the disc (White & Swank 1982). Thus in our case, the X-ray modulation can be due to the absorption by a warm absorber situated on the disc, similar to LMXBs.

In the folded light curve in Figure 3.8, the start time of radial velocities curve of Schmidtocreick et al. (2003) was used (HJD = 2452328.578335) as our epoch. The phase error 0.00004 is small enough so that our folded light curve is phase locked with radial velocity curve of Schmidtobreick et al. (2003). According to Scmidtobreick et al. (2003), there is a strong emission source opposite of the hot spot at radial phase 0.3. This phase overlaps with the phase of the X-ray

eclipse in our folded light curve at 0.3. Thus it is most likely that the eclipse is related to the emission region on the disc. This supports the idea that the reason for the X-ray modulation is the absorption by a warm absorber.

In the folded light curve where we used the eclipse time in S3464 optical light curve of Warner (1986). The error for the zero phase is 0.002 which is small enough so that it locks to the optical eclipse. The folded light curve, however does not show an eclipse at the phase 0 but rather at 0.7. So the X-ray eclipse leads the optical eclipse by 0.3 phases. This would possibly mean that the dominant X-ray and optical emitting regions are different in the system.

CHAPTER 5

CONCLUSIONS

The Spectrum of the source shows a bremsstrahlung temperature in the range 0.99 - 1.6 keV that is consistent with the bremsstrahlung temperature range of the non-magnetic CVs which is 1-5 keV (Kuulkers et. al 2006). Emission lines of the elements Fe (transitions between XVII and XXIV, (Fe L complex)), S (XIV and XVI), Ca (transitions between XV and XVII), Ne (IX, X), O (VII, VIII), C VI; and absorption lines of elements Fe (transitions between XVII and XXIV), Ne (X, IX) and Na X are consistent with the spectrum. The emission lines are in accordance with the hot thermal plasma emission as in other non-magnetic CVs. The absorption lines are most probably due to the absorption by a warm absorber on the disc. The source shows a clear modulation in X-rays in the orbital period which supports the above suggestion. It also shows a difference in photoelectric absorption in the orbital period. It is most likely that the X-ray modulation is caused by the neutral H absorption difference. Existence of the warm absorber is not conclusive.

REFERENCES

[1] Arnaud K. A., 1996, ASPC, 101, 17

[2] Baskill D.S., Wheatley P.J., Osborne J.P., 2005, MNRAS, 357, 626

[3] Buckley D. A. H., Haberl F., Motch C., Pollard K., Schwarzenberg-Czerny A., Sekiguchi K., 2007, MNRAS, 287, 117

[4] Beuermann K., Thomas H.-C., Giommi P., Tagliaferri G., Schwope A. D., 1989, A&A, 219, 7

[5] Cropper M., 1990, SSRv, 54, 195

[6] Cropper M., Ramsay G., Wu K., 1998, MNRAS, 293, 222

[7] Cropper M., Wu K., Ramsay G., 2000, New Astron. Rev., 44, 57

[8] Done C., Osborne J. P., 1997, MNRAS, 288, 649

[9] de Martino D., Matt G., Mukai K., Bonnet-Bidaud J.-M., Burwitz V., Gänsicke B. T., Haberl F., Mouchet M., 2006, A&A, 454, 287

[10] Evans P. A., Hellier C., 2007, ApJ, 663, 1277

[11] Evans P. A., Hellier C., Ramsay G., 2006, MNRAS, 369, 1229

[12] Evans P. A., Hellier C., 2004, MNRAS, 353, 447

[13] Ezuka H., Ishida M., 1999, ApJ, 120, 277

[14] Ferland G. J., Pepper G. H., Langer S. H., MacDonald J., Truran J. W., Shaviv G., 1982, ApJ, 262, 53

[15] Frank J., King A. R., Lasota J. -P., 1984, A&A, 178, 137

[16] Fruscione A., Siemiginowska A., 2000, ChNew, 7, 4

[17] Fujimoto R., Ishida M., 1997, ApJ, 474, 774

[18] Garmire, G. P., et al. 1992, in AIAA Space Programs and Technologies Conf., 8

[19] Gill, C. D., O'Brien, T. J. 1998, MNRAS, 300, 221

[20] Haefner R., Metz K., 1982, A&A, 109, 171

[21] Haefner, R., Schoembs, R., 1985, A&A, 150, 325

[22] Hamilton R. T. et al., 2007, ApJ, in press

[23] Hellier, C., 2001, "Cataclysmic Variable Stars, How and why they vary", Springer-Praxis Books in astronomy and space sciences, Cornwall

[24] Hellier C., Garlick M. A., Mason K. O., 1993, MNRAS, 260, 299

[25] Hellier C., Beardmore A. P., 2002, MNRAS, 331, 407

[26] Hellier C., Mukai K., Beardmore A. P., 1997, MNRAS, 292, 397

[27] Hellier C., Mukai K., 2004, MNRAS, 352, 1037

[28] Hellier C., Cropper M., Mason K. O., 1991, MNRAS, 248, 233

[29] Hernanz M., 2005, ASPC, 330, 265

[30] Kubiak, M., 1984, Acta Astron., 34, 331

[31] Kuulkers E., Norton A., Schwope A., Warner B., 2006, in "Compact stellar X-ray sources", eds. Lewin W. & van der Klis M., vol 39., p. 421 - 460

[32] Lamb D. Q., Masters A. R., 1979, ApJ, 234, 117

[33] King A. R., Lasota J. -P., 1979, MNRAS, 188, 653

[34] King A. R., Lasota J. -P., 1990, MNRAS, 247, 214

[35] Mauche C. W., Raymond J. C., 2000, ApJ, 541, 924

[36] Mauche C. W., Robinson E. L., 2001, ApJ, 562, 508

[37] Mason K. O., Drew J. E., Knigge C., 1997, MNRAS, 290, 23

[38] McNamara A. L., Kuncic Z., Wu K., Galloway D. K., Cullen J. G., 2007, arXiv, 0704, 1516

[39] Meyer F., Meyer-Hofmeister E., 1994, A&A, 288, 175

[40] Mukai K, Wood J. H., Naylor T., Schlegel, E. M., Swank, J., 1997, ApJ, 475, 812

[41] Mukai K., 2000, NewAR, 44, 9

[42] Mukai K., Kallman T., Schlegel E., Bruch A., Handle G., Kemp J., 2001, ASPC, 251, 90

[43] Mukai K., 2003, AdSpR, 32, 2067

[44] Mukai K, Kinkhabwala A., Peterson J. R., Kahn S. M., Paerels F., 2003, ApJ, 586, 77

[45] Mukai K., 2005, ASPC, 330, 147

[46] Mushotzky R.F., Szymkowiak A.E., 1988, in: Cooling flows in clusters and galaxies, ed: Fabian A.C., Kluwer Dordrecht, the Netherlands, 53

[47] Naylor T., la Dous C., 1997, MNRAS, 290, 160

[48] Nelemans G., 2005, ASPC, 334, 643

[49] Norton A. J., Watson M. G., 1989, MNRAS, 237, 715

[50] Norton A. J.,Beardmore A. P., Allan A., Hellier C., 1999, A&A, 347, 203

[51] Norton A. J., Somerscales R. V., Wynn G. A., 2004, ASPC, 315, 216

[52] Osaki Y., 1996, PASP, 108, 390

[53] Pandel D., Córdova F. A., Mason K. O., Priedhorsky W. C., 2005, ApJ, 626, 396

[54] Patteron J., 1994, PASP, 106, 209

[55] Patterson J., Raymond J.C., 1985, ApJ, 292, 535

[56] Pratt G. W., Mukai K., Hassall B. J. M., Naylor T., Wood J. H., 2004, MNRAS, 348, 49

[57] Pringle J.E., 1981, ARA&A, 19, 137

[58] Rana V. R., Singh K. P., Schlegel E.M., Barret P. E., 2004, AJ, 127, 439

[59] Rana V. R., Singh K. P., Schlegel E.M., Barret P. E., 2006, ApJ, 642, 1042

[60] Rana V. R., Singh K. P., Schlegel E.M., Barret P. E., 2006, AdSpR, 38, 284

[61] Ramsay G., Mason K. O., Cropper M., Watson M. G., Clayton K. L., 1994, MNRAS, 270, 692

[62] Ramsay G., Cropper M., 2004, MNRAS, 347, 497

[63] Ramsay G., Cropper M., Wu K., Mason K. O., Cordova F. A., 2004, MNRAS, 350, 1373

[64] Ramsay G., Poole T., Mason K., Cordova F., Priedhorsky W., Breeveld A., Much R., Osborne J., Pandel D., Potter S., West J., Wheatley P., 2001, A&A, 365, 288

[65] Ramsay G., Bridge C. M., Cropper M., Mason K. O., Cordova F. A., Priedhorsky W., 2004, MNRAS, 354, 773

[66] Raymond J. C., Brickhouse N. S., 1996, ApJ, 237, 321

[67] Ribeiro F. M. A., Diaz M. P., 2006, PASP, 118, 84

[68] Richman H. R., 1996, ApJ, 462, 404

[69] Shakura N. I., Sunyaev R. A., 1973, A&A, 24, 337

[70] Schmidtobreick, L. et al., 2006, in: Close Binaries in the 21st Century: New Opportunities and Challenges, Astroph. Space Sci., 304, 303

[71] Schwarz R., Reinsch K., Beuermann K., Burwitz V., 2005, A&A, 442, 271

[72] Schwope A. D., Schwarz R., Sirk M., Howell S. B., 2001, A&A, 375, 419

[73] Singh K. P., Rana V. R., Mukerjee K., Barrett P., Schlegel E. M., 2004, ASPC, 315, 135

[74] Singh K., White, N. E., Drake S. A., 1996, ApJ, 456, 766

[75] Smith R. C., 2007, arXiv:astro-ph/0701654v1

[76] Stella L., Angelini L., 1992, ASPC, 25, 103

[77] Szkody P., Nishikida K., Raymond J. C., Seth A., Hoard D. W., Long K. S., Sion E. M., 2002, ApJ, 574, 942

[78] Szkody P., Homer L., Chen B., Henden A., Schmidt, G. D., Anderson S. F., Hoard D. W., Voges W., Brinkmann J., 2004, AJ, 128, 244

[79] Terada Y., Ishida M., Makishima K., 2004, PASJ, 56, 533

[80] Verbunt F., 1982, SSRv, 32, 379

[81] van der Woerd H., Heise J., Bateson F., 1986, A&A, 156, 252

[82] van Teeseling A., Beuermann K., Verbunt F., 1996, A&A, 315, 467

[83] van Teeseling A, 1997, A&A, 319, 25

[84] van Teeseling A, Verbunt F., 1994, A&A, 292, 519

[85] Vogt N., 1975, A&A, 41, 15

[86] Warner B., 1986, MNRAS, 219, 751

[87] Warner B., Livio M., Tout C., 1996, MNRAS, 282, 735

[88] Warner B., 1995, "Cataclysmic Variable Stars", Cambridge Univ. Press, Cambridge

[89] Weisskopf M. C., O'dell S. L., van Speybroeck L. P., 1996, SPIE, 2805, 2

[90] Wheatley P. J., West R. G., 2003, MNRAS, 345, 1009

[91] Wheatley P. J., Mauche C. W., Mattei J. A., 2003, MNRAS, 345, 49

[92] White N. E., Swank J. H., 1982, ApJ, 253, 61

[93] Wu K., 2000, SSRv, 93, 611